



ELSEVIER

Physica D 108 (1997) 236–276

PHYSICA D

Absolute and convective instabilities, front velocities and global modes in nonlinear systems

Arnaud Couairon *, Jean-Marc Chomaz

*LadHyX, CNRS UMR 156, Laboratoire d'Hydrodynamique, École Polytechnique,
91 128 Palaiseau Cedex, France*

Received 23 October 1996; accepted March 1997

Communicated by S. Fauve

Abstract

We study the existence of self-sustained saturated solutions of the real Ginzburg–Landau equation subject to a boundary condition at $x = 0$; such solutions are called nonlinear global (NG) modes. The NG instability referring to the existence of these solutions is rigorously determined and the scaling behavior of the NG modes close to threshold is derived. The NG instability is first compared to the linear concept of convective/absolute (C/A) instability characterizing whether the impulse response of an unstable flow in an infinite domain is asymptotically damped or amplified at a fixed location. NG modes are shown to exist while at the same time the flow may be linearly stable, convectively unstable, or absolutely unstable. The growth size of the NG modes is shown to be proportional to $\epsilon^{-1/2}$ when NG and A instabilities exist simultaneously, ϵ being the criticality parameter, whereas a $\ln(1/\epsilon)$ scaling is found when the NG instability occurs while the flow is C unstable or linearly stable.

The nonlinear convective/absolute (NC/NA) instability defined Chomaz (1992) by considering, in infinite homogeneous domains, whether the front separating a bifurcated state from the basic state moves downstream or upstream, is determined using van Saarloos and Hohenberg (1992) results for the selected front velocity. Remarkably, the NA domain and the NG domain are shown to coincide. Similar results are presented for supercritical bifurcating systems, for the “van der Pol–Duffing” system, and for a transcritical model. In all the cases, the A instability is only a sufficient condition for the existence of an NG mode, and these simple models demonstrate that a system may be nonlinearly absolutely unstable whereas it is linearly convectively unstable. This property should be generic if one accepts the conjecture that the selected front velocity is always larger than the linear front velocity.

Response to a constant forcing applied at the origin is also studied. It is shown that in the NG region, the system possesses intrinsic dynamics which cannot be removed by the forcing. By contrast, the behavior of a nonlinear spatial amplifier is observed in a domain larger than the NC region. NC instability is only a sufficient condition to trigger the system with forcing.

* Corresponding author. Tel.: 33-1-69 33 37 28; fax: 33-1-69 33 30 30; e-mail: couairon@ladhyx.polytechnique.fr.

1. Introduction

The concepts of linear absolute (A) and convective (C) instabilities have recently been applied to understand the spatiotemporal development of open flows such as mixing layers, jets, or wakes [1–3]. In these flows fluid particles continuously enter and leave the experimental domain of interest. Therefore, the input perturbations and the mean advection have to be taken into account explicitly. The concepts of linear absolute or convective instability are usually defined with respect to the linear response to an initially localized impulse perturbation. If the wave packet, representing the Green function, asymptotically decays in any uniformly translating frame, the system is said to be linearly stable (S) (Fig. 1(a)). If this is not the case, it is linearly unstable. Moreover, it is linearly absolutely (A) unstable if, at any fixed location, the response grows in time (Fig. 1(c)) and linearly convectively (C) unstable if it decays (Fig. 1(b)). In a C unstable system, perturbations grow as they are advected away and the system acts as a spatial amplifier of incoming turbulence. On the contrary, in an A unstable system, perturbations viewed at a fixed location keep growing and the system is thought to ultimately exhibit an intrinsic self-sustained oscillation.

In the linear approximation, such a self-sustained oscillation has been analyzed by Chomaz et al. [4–6], Huerre and Monkewitz [1], Monkewitz et al. [7], le Dizès et al. [8], Hunt and Crighton [9,10]. It has been called a linear

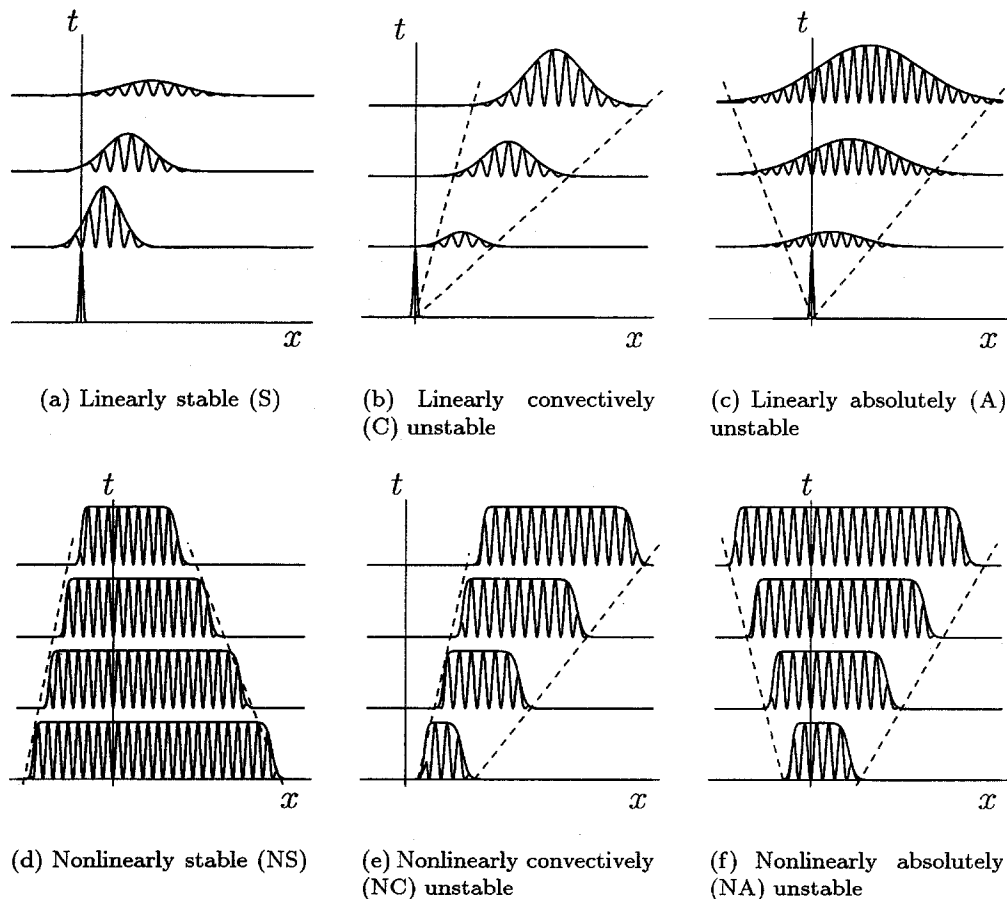


Fig. 1. Sketches of the typical response of the system in the (x, t) plane.

global mode because it develops over the whole spatial domain, requiring the resolution of an eigenproblem, not only in the transverse direction, but also in the direction of the flow (x). Inhomogeneity in x (variation of the basic flow in x or boundary condition) is a necessary condition for the existence of linear global modes. When the inhomogeneity is weak (slow variation of the length scale λ , i.e. $d \log \lambda / dx \equiv \epsilon \ll 1$), a WKBJ approximation may be used to show that the existence of a local absolute region in the flow is a necessary condition for the occurrence of an unstable linear global mode. In fact, resonances observed in real experiments such as a flow past a cylinder, a helium hot jet [11], or a mixing layer with a back flow [12] are likely to result from the nonlinear saturation of a global mode. The weakly nonlinear theory has been applied to linear global modes [6,8,13] but, despite the already strong but inherent limitation that the amplitude must be exponentially smaller than the inhomogeneity parameter ϵ for the theory to be valid, it has been shown (Le Dizès et al. [8]) to be ill-posed and the determination of the nonlinear nature of the bifurcation is in general impossible as ϵ goes to zero. The physical explanation of this mathematical breakdown is that, for an order-1 advection velocity, the nonlinear modification of the basic flow occurs far downstream of the region which determines the growth rate of the linear global mode. Technically, this corresponds to the fact that, at the global instability threshold, the eigenfunctions of the linearized inhomogeneous operator and its adjoint do not overlap. This failure of the weakly nonlinear route signals the need for a strongly nonlinear analysis of the absolute and convective instability concepts.

In this spirit, Chomaz [14] has extended the notions of absolute and convective instabilities to nonlinearly unstable systems. This notion may be important not only for the description of nonlinearly unstable open flows such as boundary layers or Poiseuille flow, but also for linearly unstable flows with order-one advection for which the absolute instability occurs far from “the” threshold. For these systems where Galilean invariance is broken and the laboratory frame is unambiguously specified, nonlinear absolute and convective instabilities have been defined as follows: “The basic state of a system is *nonlinearly stable* (NS) if for all initial perturbations of finite extent and amplitude, the system relaxes to the basic state everywhere in any moving frame. The system is unstable if it is not stable in the above sense. The instability is *nonlinearly convective* (NC) if, for all initial perturbations of finite extent and finite amplitude, the system relaxes to the basic state everywhere in the laboratory frame. It is *nonlinearly absolute* (NA) if, for some initial condition of finite extent and amplitude, the system does not relax to the basic state everywhere in the laboratory frame”. In the above definition, the “laboratory frame” refers to an experimental situation and is used to point out the frame specified by boundary conditions, forcing, etc.

A more convenient definition has been given in [14] for a one-dimensional bifurcating system *in an infinite domain*. The nonlinear nature of the instability may be determined by referring to the evolution of an initial “droplet” of bifurcating state surrounded by the basic state. When all initial droplets shrink (Fig. 1(d)) the system is stable; when at least one droplet expands (Figs. 1(e) and (f)) the system is nonlinearly unstable. In this case, the distinction between absolute and convective instability depends on the velocity of the fronts limiting the droplet “in the laboratory frame”. When the two limiting fronts are moving in the same direction, the instability is NC (Fig. 1(e)) and it is NA when the fronts are moving in opposite directions (Fig. 1(f)).

If we keep the usual convention that the mean advection is directed to the right, the convective or absolute instability is solely discriminated by the direction of propagation of the trailing front. In the abundant literature about fronts, the front velocity V_f is usually oriented from the bifurcated region to the basic state. Here V_f is thus positive when front moves to the left and negative when it moves to the right (V_f being oriented from right to left). Using this convention, the nonlinearly absolute or convective nature of the instability is determined by the sign V_f as follows: when $V_f > 0$ ($V_f < 0$), the front moves to the left (right) in the “laboratory” frame, thus the flow is NA (NC) unstable. If the uniformly translating “front” solution is not unique, the determination of V_f implies the solution of a selection problem recently elucidated by Dee [15,16], Ben-Jacob et al. [17], and van Saarloos and Hohenberg [18–20] among others. In particular, van Saarloos and Hohenberg [18] have formulated the principle that the nonlinearly selected front velocity V_f is always greater than the velocity V_f^1 of the linearly selected front. As

pointed out by Huerre and Monkewitz [1], V_f^1 is the velocity of the trailing edge of the Green function. Therefore, the sign of V_f^1 determines whether the instability is *linearly absolute* ($V_f^1 > 0$ with our orientation convention) or *linearly convective* ($V_f^1 < 0$). The principle of van Saarloos and Hohenberg's essentially implies the extremely important property, illustrated by the present paper that A instability is only a sufficient condition for NA instability. Indeed, if the system is A unstable then $V_f^1 > 0$, but as $V_f > V_f^1$, we immediately deduce that $V_f > 0$, which implies that the system is NA unstable. The converse is false since there may exist domains of the parameter space where the flow is linearly stable or linearly convectively unstable but nonlinearly absolutely unstable (see Section 2).

The previous definitions pertain to the ideal case of an infinite domain with a somewhat artificial introduction of the laboratory frame. Dealing with real open flows, as argued by Huerre and Monkewitz [1] and Chomaz and coworkers [4,14], the useful concept is the existence of a global mode of the flow which takes into account the upstream and downstream boundary conditions (eventually the lateral boundary conditions) and the nonparallelism of the flow. This global instability leads to self-sustained dynamics characterizing the intrinsic behavior of the flow. In the linear approximation, the linear global instability corresponds to the emergence of a temporally growing solution occupying the whole spatial domain (the linear global mode). In a fully nonlinear study [21], the nonlinear global (NG) instability will correspond to the existence of a saturated solution of the original problem (the nonlinear global mode).

The physical significance of these notions will be illustrated by considering one-dimensional systems *in a semi-infinite domain*, with homogeneous left boundary conditions. A semi-infinite domain represents an idealized open flow, in which the perturbation level is supposed to be zero at the entrance of the test section. Galilean invariance is actually broken by the left boundary condition, which unambiguously singles out the laboratory frame.

The aim of the present study is to establish the link between A, NA, and NG instabilities for simple one-dimensional systems. For this purpose, we consider the one-dimensional real Ginzburg–Landau equation

$$\frac{\partial A}{\partial t} + U_0 \frac{\partial A}{\partial x} = \frac{\partial^2 A}{\partial x^2} - \frac{\delta \mathcal{V}(A)}{\delta A}, \quad (1)$$

where A stands for the real amplitude of the bifurcating mode. The operator $U_0 \partial A / \partial x$ represents the effect of advection at the mean velocity U_0 (taken positive). Except for the last section of our paper, the potential density $\mathcal{V}(A)$ is taken in the form

$$\mathcal{V}(A) = -\mu \frac{A^2}{2} - \frac{A^4}{4} + \frac{A^6}{6}, \quad (2)$$

which gives rise to a subcritical pitchfork bifurcation. In this case, Eqs. (1) and (2) depend on two independent constant control parameters: the advection velocity U_0 and the bifurcation parameter μ .

The outline of the paper is as follows. In Section 2, we give a brief review of the concepts ruling the propagation of fronts separating the bifurcating state from the basic state. This allows us to delineate the S, C, A, NS, NC and NA regions of parameter space for model equation (1) with potential density (2). Although this section is a straightforward application of Chomaz's definition to van Saarloos and Hohenberg's results, the front solutions and the selection mechanism are presented because their phase-space interpretation also governs the existence of the NG mode. The latter problem is addressed in Section 3 where the NG solutions of (1) and (2) in a semi-infinite domain with homogeneous boundary conditions at the origin ($x = 0$) are derived. Remarkably, we find that the existence region of such an NG mode, rigorously demonstrated by a perturbation argument, coincides with the NA region defined from the front velocity selection criterion. The NG mode existence demonstration gives us information which has no equivalent in the front selection problem. In particular, we obtain in this manner scaling laws for the growth size of the NG mode which appear to be remarkably different depending on whether the NG instability threshold precedes the A instability threshold or coincides with it. The multiplicity of global modes is mentioned

and the stability of all global modes is determined numerically. The response of (1) to an excitation of constant amplitude applied at the origin is examined in Section 4 where it is demonstrated that the system acts as a spatial nonlinear amplifier in the NC region. In Section 5, we verify the genericity of the above results by examining two other potential densities $\mathcal{V}(A)$ corresponding to a supercritical bifurcation and to a transcritical bifurcation that breaks the $A \rightarrow -A$ symmetry, and by considering the case of the van der Pol–Duffing-like system with an additional nonlinear term $A^2\partial A/\partial x$ in (1). In particular, we demonstrate that even for a supercritical bifurcation, the system may become NG unstable in regions of parameter space where the instability is C.

We recall here the set of abbreviations we are going to use throughout this paper: S, C, A denote linearly stable, linearly convective, and linearly absolute, respectively. NS, NC, NA denote nonlinearly stable, nonlinearly convective, and nonlinearly absolute, respectively. All these notions refer to an infinite domain and only NG, denoting nonlinear global, refers to the semi-infinite domain.

2. Front propagation and absolute instabilities

For the sake of clarity, it is convenient to emphasize once more the distinction between the *laboratory frame* in which the mean advection velocity is U_0 , oriented to the right and the *advected frame* with no mean advection. We then describe the different possible fronts by their velocity v_f in the advected frame and V_f in the laboratory frame, oriented from right to the left. We recall that this somehow nonintuitive orientation is identical to the one classically adopted in the literature with v_f taken positive when pointing from the bifurcated region to the basic state region. In front studies, the bifurcated region is located to the left but in our case, the mean flow being taken to the right, the front we have to consider for the NC/NA instability determination separates the basic state on the left from the bifurcated state on the right. To preserve the mean flow classical orientation and the results from the front literature, we have decided to adopt this counter intuitive orientation for v_f and V_f . In the alternative, we would have been obliged to transform all the results from the front literature carrying unpractical minus sign in all the formulas. The velocity v_f is connected to its counterpart V_f in the laboratory frame, through the relation

$$v_f = U_0 + V_f \tag{3}$$

2.1. Front velocity selection criteria: A concise review

In the Rayleigh–Bénard experiment, when the temperature difference between the upper and the lower surface of the fluid layer is abruptly increased above threshold, the convection establishes itself by displacement of a convection front which is correctly determined by the theory developed below [22]. Similar phenomena occur in a Couette–Taylor flow. When the rotation rate is abruptly increased, the bifurcating state starts invading the diffusing state from the boundary forming a vortex front experimentally studied by Ahlers and Cannel [23] and numerically by Lücke et al. [24]. Front propagation also appears in chemical reactions as shown by Hanna et al. [25] or in population genetics [26]. The determination of the front velocity in these various configurations and the analysis of the related pattern selection mechanism has motivated a whole group of theoretical studies. In particular, linear and nonlinear theories for front propagation have been developed [15–17,19,20]. The measurement of front velocities by Fineberg and Steinberg [22] and by Ahlers and Cannel [23] are in good agreement with the linear predictions. The nonlinear theory is not a pathological mathematical case and its validity has been experimentally illustrated in the work of Hanna et al. [25] on chemical waves in the iodate oxydation of arsenous acid systems. Their measurements of front velocities correspond to the nonlinear predictions of the transcritical model of Section 5.3. Palffy-Muhoray

et al. [27] also measured front velocities corresponding to the nonlinear predictions of the subcritical model in a nematic liquid crystal.

The mathematical analysis of Eq. (1) by Aronson and Weinberger [26,38] demonstrates that for a large class of potential functions $\mathcal{V}(A)$ and for sufficiently localized initial conditions the front velocity asymptotically approaches a constant value v_f . Dee [15,16], Ben-Jacob et al. [17], and van Saarloos [19,20] showed that this selected velocity corresponds to neutrally stable linear perturbations in the reference frame moving with the front. Huerre and Monkewitz [1] noticed that this problem is equivalent to the determination of the trailing edge velocity of the linear wave packet issuing from an impulsive initial perturbation (Green function). For a system invariant with respect to time translation and space translation in the x -direction, the linear dynamics is described by a dispersion relation

$$D(\omega, k) = 0, \tag{4}$$

where ω and k are the complex frequency and complex wave number corresponding to a Fourier mode of the form $e^{i(kx-\omega t)}$. On each ray moving at velocity v to the left $x/t = -v$ in the (x, t) plane¹ (see Fig. 1), the asymptotically selected wave (k^v, ω^v) is such that²

$$D(\omega^v, k^v) = 0, \tag{5}$$

$$\frac{\partial D/\partial k}{\partial D/\partial \omega}(\omega^v, k^v) = v. \tag{6}$$

On this ray, the growth rate equals

$$\sigma(v) = \omega_i^v + k_i^v v. \tag{7}$$

The trailing edge of the wave packet corresponds to the ray $x/t = -v^l$ on which the selected wave is neutral: $\sigma(v^l) = 0$. Therefore, the linearly selected front moves at velocity v^l .

Van Saarloos [19,20] has noticed that for sufficiently localized initial conditions, “nonlinear” marginal stability may select a faster nonlinear front. van Saarloos and Hohenberg [18] have formulated the following conjecture: nonlinear selection occurs when there exists a discrete front with a velocity v^{nl} and a spatial decay rate³ k_i^{nl} satisfying

$$v^l < v^{nl} \quad \text{and} \quad |k_i^l| < |k_i^{nl}|. \tag{8}$$

This conjecture allows van Saarloos and Hohenberg to determine explicitly the front velocity of the complex Ginzburg–Landau equation.

2.2. Front solutions in the real Ginzburg–Landau equation

In this section, we describe uniformly translating fronts for the real Ginzburg–Landau equation. The profusion of details that follow might appear unnecessary as we only recover published results [15–17,19,20,28,29] in this section but the precise description of the phase space structure corresponding to the front solutions will be necessary for the determination of the global modes in Section 3.

Let us recall some classical results [28] on the real Ginzburg–Landau model (1) and (2).

¹ The minus sign comes from the convention for the sign of front velocity which is positive when the front moves toward the x negative.
² The supplementary pinching condition is not developed here (see [1]).
³ k_i^{nl} is defined as $(1/A) dA/dx$ at $x \rightarrow -\infty$. Although its value may be determined by linearizing an amplitude equation around the basic state, k_i^{nl} depends on the properties of the front solution in the whole domain as illustrated in Section 2.2, since the nonlinear selection involves the whole domain.

In the “advected” frame with $U_0 = 0$, Eq. (1) reads

$$\frac{\partial A}{\partial t} = \frac{\partial^2 A}{\partial x^2} - \frac{\delta \mathcal{V}(A)}{\delta A}, \quad (9)$$

and admits a Lyapunov functional \mathcal{L}

$$\mathcal{L}(A) = \int \left[\frac{1}{2} \left(\frac{\partial A}{\partial x} \right)^2 + \mathcal{V}(A) \right] dx. \quad (10)$$

One notes that \mathcal{L} is minimum for uniform solutions that minimize the potential density $\mathcal{V}(A)$ given by (2). When $\mu < -1/4$, $A_0 \equiv 0$ is the single minimum. When $-1/4 < \mu < 0$, there exists three minima at $A_0 \equiv 0$ and $A_2 \equiv \pm(1/2 + \sqrt{\mu + 1/4})^{1/2}$. The amplitudes $A_1 \equiv \pm(1/2 - \sqrt{\mu + 1/4})^{1/2}$ correspond to a maximum of $\mathcal{V}(A)$ and therefore to a linearly unstable solution. The parameter value $\mu_M = -3/16$ defines the Maxwell point at which the solutions A_0 and A_2 possess equal potential density. When $\mu_M < \mu < 0$, A_0 is said to be metastable (M) and A_2 is stable (S): a droplet of state A_2 embedded in an ocean of basic state A_0 expands. When μ passes 0, A_0 becomes a maximum of $\mathcal{V}(A)$, i.e. unstable, A_1 disappears, and A_2 becomes the only stable solution.

A front represents a uniformly translating solution moving at velocity v of the form⁴ $A(x + vt)$. The front velocity satisfies the nonlinear eigenvalue problem

$$v \frac{dA}{dx} = -\frac{\delta \mathcal{V}}{\delta A} + \frac{d^2 A}{dx^2} \quad (11)$$

with boundary conditions

$$A(-\infty) = A_0 = 0, \quad A(+\infty) = A_2. \quad (12)$$

As noticed by many authors [15–17,19,20], for Eq. (11) with boundary conditions (12), the eigenvalue v is not unique and one has to determine which one is dynamically selected. In the phase space $(A, dA/dx)$, front solutions correspond to a heteroclinic orbit linking the basic state A_0 to the bifurcated state A_2 . The front corresponding to the linear selection criterion [18] possesses the velocity $v^1(\mu)$ and a spatial decay rate $k_i^1(\mu)$ given by $\sigma(v^1) = 0$ where $\sigma(v)$ is given by (7) and $D(\omega, k) = -i\omega + k^2 - \mu$:

$$v^1(\mu) = 2\sqrt{\mu}; \quad k_i^1(\mu) = -\sqrt{\mu}. \quad (13)$$

The linear front selection may only hold for $\mu > 0$. For the determination of nonlinear fronts, we have to describe the trajectories of (11) in the phase space. Phase portraits can be obtained by using a mechanical analogy. When x is formally interpreted as $-t$, Eq. (11) may be viewed as a dynamical system for a particle in a potential $-\mathcal{V}(A)$ with friction coefficient v . A detailed description of the phase portrait is given in Appendix A. Only general trends are discussed below, typical phase portraits being presented in Fig. 2. The arrows indicate increasing x and should be inverted according to the transformation $x \rightarrow -t$ when the particle analogy is used. The real orbits have been computed by a variable step Runge–Kutta integration of the associated first-order differential system

$$\frac{dA}{dx} = u, \quad (14a)$$

$$\frac{du}{dx} = vu + \frac{\delta \mathcal{V}}{\delta A}. \quad (14b)$$

⁴ By convention, the front velocity is oriented to the left whereas x is oriented to the right. This explains the unusual plus sign in $A(x + vt)$.

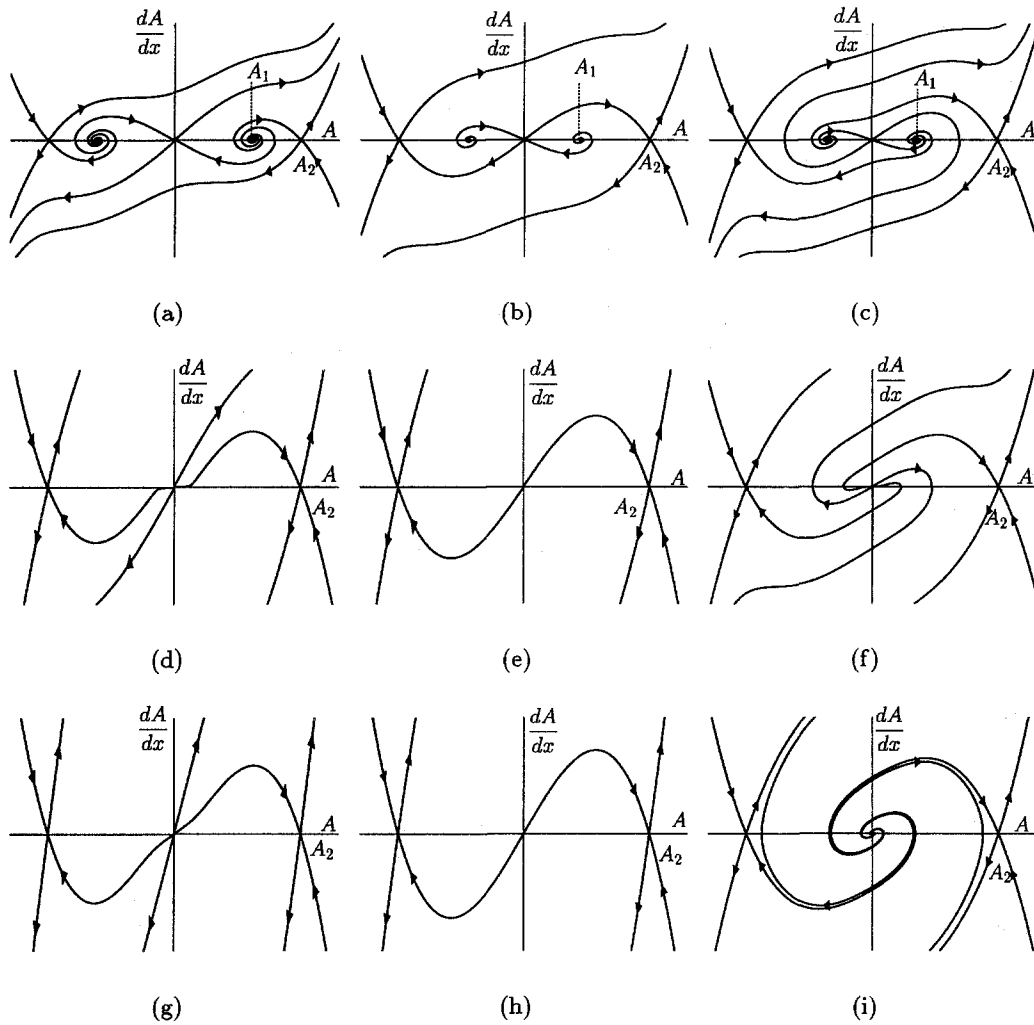


Fig. 2. Phase portraits pertaining to a specific region of parameter space in Fig. 3: Each line corresponds to a constant value of μ and a decreasing velocity from left to right. (a)–(c): $\mu < 0$. (d)–(f): $0 < \mu < 3/4$. (g)–(i): $\mu > 3/4$. In the first column (a), (d) and (g) correspond to the white region in Fig. 3; in the second column, (b) corresponds to the line $v^{nl}(\mu)$ for $\mu < 0$, (e) corresponds to the line $v^{nl}(\mu)$ for $0 < \mu < 3/4$, and (h) corresponds to the line $v^l(\mu)$ for $\mu > 3/4$. In the third column, (c) corresponds to the light gray region, (f) to the medium gray region and (i) to the dark gray region in Fig. 3.

Unstable manifolds are obtained using forward x -integration whereas stable manifolds are obtained by backward integration. The front solution exists when the stable manifold of A_2 (asymptotic to A_2 as $x \rightarrow +\infty$) connects to A_0 to form an heteroclinic orbit. In the following, the shape of this manifold in the phase space of dynamical system (14a) and (14b) is discussed. Each phase portrait presented in Fig. 2 is typical of a region in parameter space (see Fig. 3).

Metastable region $\mu_M < \mu < 0$. At fixed μ , the stable manifold of A_2 issues from A_1 (Fig. 2(a)). For a particular value v_1 of v (Fig. 2(b)), the stable manifold of A_2 connects with the unstable manifold of A_0 . Below v_1 (Fig. 2(c)), it comes spiraling out from $-A_1$. For a still lower particular value v_2 , the stable manifold of A_2 connects from the $A < 0$ side to the unstable manifold of A_0 ; below v_2 , the trajectory ending at A_2 comes from A_1 . This sequence repeats itself indefinitely, each change between an origin at $-A_1$ and A_1 being separated by a particular value v_n

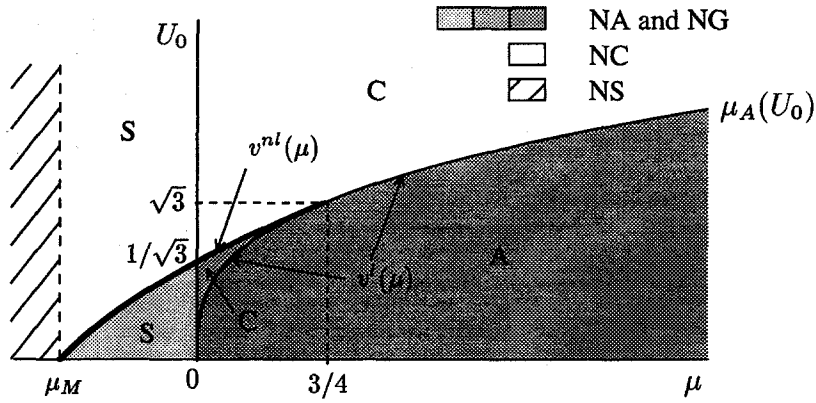


Fig. 3. Nonlinearly absolutely (NA) unstable domain (shaded regions) in parameter space. The dark gray region represents the linearly absolutely (A) unstable region which is totally embedded in the NA region. The system is NA unstable in the medium and light gray regions whereas it is linearly convectively unstable (C) or linearly stable (S). The system is nonlinearly convectively (NC) unstable in the white region. The nonlinearly stable (NS) region ($\mu < \mu_M$ where $\mu_M = -3/16$ is the Maxwell point) is totally embedded in the linearly stable (S) region. Section 3 will show that an NG mode exists in the three shaded regions.

for which the stable manifold of A_2 connects with the unstable manifold of A_0 , with $n - 1$ about turns around A_0 . This multiplicity of solutions may appear strange when considering the saddle structure of A_0 . However, it may be easily checked by using the mechanical analogy. We leave it to the reader to transpose the discussion in terms of this mechanical analogy. Therefore, for $\mu_M < \mu < 0$, one has to solve a *discrete* selection problem since the heteroclinic orbits linking A_0 at $x = -\infty$ to A_2 at $x = +\infty$ exist for ordered discrete values v_n .

According to the conjecture of van Saarloos and Hohenberg, the selected front is the *fastest front with the steepest fallout*: it corresponds to the heteroclinic orbit depicted in Fig. 2(b), associated with the velocity v_1 and therefore called v^{nl} . In Fig. 3, the selected front velocity is represented by the heavy curve $v^{nl}(\mu)$ that separates white and gray domains. The corresponding particular solution may be sought in terms of a polynomial solution for $u(A) = dA/dx$, which satisfies

$$u \frac{du}{dA} - vu - \frac{\partial V}{\partial A} = 0, \tag{15}$$

with the boundary conditions

$$u(A_0) = 0, \quad u(A_2) = 0. \tag{16}$$

As found by van Saarloos and Hohenberg, this solution only exists for the particular value v^{nl}

$$v^{nl}(\mu) \equiv v_1(\mu) \equiv -\sqrt{3} + \frac{4}{\sqrt{3}}(A_2(\mu))^2, \tag{17}$$

and it reads

$$u(A) = \frac{1}{\sqrt{3}}A(A_2^2 - A^2). \tag{18}$$

This nonlinear front is associated with an asymptotic spatial decay rate given by

$$k_i^{nl}(\mu) \equiv - \left. \frac{du}{dA} \right|_{A_0} = -\frac{1}{\sqrt{3}}(A_2(\mu))^2. \tag{19}$$

Linearly unstable region $\mu > 0$. It is quite remarkable that the above defined nonlinear front solution found for $\mu < 0$ persists for $\mu > 0$. The nonlinear and linear velocity curves $v^{\text{nl}}(\mu)$ and $v^{\text{l}}(\mu)$, plotted in Fig. 3, are tangent at $\mu = 3/4$. Therefore, we distinguish between three regions of (v, μ) space as defined in Fig. 3:

- White region where $v > v^{\text{nl}}(\mu)$ if $0 < \mu < 3/4$ and $v > v^{\text{l}}(\mu)$ if $\mu > 3/4$. In this region of parameter space, the corresponding stable manifold of A_2 issues, for any value of v , from A_0 without spiraling out (Figs. 2(d) and (g)).
- Medium gray region where $v^{\text{l}}(\mu) < v < v^{\text{nl}}(\mu)$ in the range $0 < \mu < 3/4$. The heteroclinic orbit ending at A_2 comes from A_0 after a finite number of turns around A_0 (Fig. 2(f)). Note that this number increases when parameters approach the curve $v^{\text{l}}(\mu)$ delineating the dark gray region. Again, this multiplicity may appear strange when considering the node structure of A_0 , but it is easily checked with the mechanical analogy. As in the light gray region, in the part of the medium gray region between v_n and v_{n+1} , fronts makes n half about turns around A_0 .
- Dark gray region where $v < v^{\text{l}}(\mu)$. The fixed point A_0 of Eq. (11) is an unstable focus and the heteroclinic orbit ending at A_2 comes from A_0 after an infinite number of revolutions around A_0 (Fig. 2(i)).

Therefore, for $\mu > 0$, an heteroclinic orbit linking A_0 to A_2 is associated to a front solution for every value of v . The selection problem is *continuous* in contrast with the discrete selection problem prevailing in the range $\mu_{\text{M}} < \mu < 0$. Whatever μ , we have $v^{\text{nl}}(\mu) > v^{\text{l}}(\mu)$ but for $\mu < 3/4$, the nonlinear front falls off faster than its linear counterpart ($|k_i^{\text{nl}}(\mu)| > |k_i^{\text{l}}(\mu)|$) and the nonlinear front is selected following the conjecture of van Saarloos and Hohenberg. On the contrary, for $\mu > 3/4$, the linear front is selected as $|k_i^{\text{nl}}(\mu)| < |k_i^{\text{l}}(\mu)|$.

2.3. Linear absolute instability, nonlinear absolute instability and front velocities

Let us now introduce the laboratory frame characterized by a mean advection U_0 different from zero. As argued in Section 1, the sign of the linear front velocity in the laboratory frame $V^{\text{l}} = v^{\text{l}} - U_0$ determines whether the instability is linearly convective or absolute. Therefore, the curve $U_0 = v^{\text{l}}(\mu)$ delineates the linearly absolutely unstable region (in dark gray on Fig. 3). This curve corresponds to the NA instability threshold only when the linear front is selected, i.e. when $\mu > 3/4$. When $\mu_{\text{M}} < \mu < 3/4$, the nonlinear front is selected and the curve $U_0 = v^{\text{nl}}(\mu)$ defines the transition between NC and NA instability regions.

Note that, in this NA region, the system is linearly stable when $\mu_{\text{M}} < \mu < 0$ (light gray region in Fig. 3), C when $v^{\text{l}}(\mu) < U_0 < v^{\text{nl}}(\mu)$ (medium gray region in Fig. 3) and A when $U_0 < v^{\text{l}}(\mu)$ (dark gray region in Fig. 3). For this model, we verify that the region A is embedded within the NA region.

Up to now, we have fixed μ and determined the nature of the instability as a function of U_0 , but as U_0 and μ may be viewed as two independent control parameters of the system, it may be more convenient to consider U_0 constant and determine the value $\mu_{\text{A}}(U_0)$ that defines the threshold between NC and NA. The expression $\mu_{\text{A}}(U_0)$ obtained from the laws (13) and (17) for the selected front velocity reads

$$\text{if } U_0 < \sqrt{3}, \quad \mu_{\text{A}}(U_0) = \mu^{\text{nl}}(U_0) = \frac{3}{16} \left(U_0^2 - \frac{2}{\sqrt{3}} U_0 - 1 \right), \quad (20a)$$

$$\text{if } U_0 > \sqrt{3}, \quad \mu_{\text{A}}(U_0) = \mu^{\text{l}}(U_0) = \frac{U_0^2}{4}. \quad (20b)$$

The curve $\mu^{\text{nl}}(U_0)$ defines the NC/NA transition for $U_0 < \sqrt{3}$ and has no specific significance for $U_0 > \sqrt{3}$. Whatever U_0 , the curve $\mu^{\text{l}}(U_0)$ corresponds to the C/A transition but to the NC/NA transition only for $U_0 > \sqrt{3}$.

3. Nonlinear global modes in a semi-infinite domain

3.1. Nonlinear global modes and nonlinear absolute instability

We consider stationary solutions of (1) in a semi-infinite domain with $U_0 \neq 0$ and boundary condition $A(0) = 0$. As we have already noticed, this boundary condition breaks the Galilean invariance and unambiguously singles out the laboratory frame. Actually, it represents an idealized flow in which no disturbances are present at the entrance of the domain. For real flows, more realistic, but inevitably more complicated, boundary conditions should be studied case by case to see if our idealized solutions persist. An example will be given in Section 4 for the signaling problem. Nontrivial stationary solutions satisfy the equation

$$\frac{d^2 A}{dx^2} - U_0 \frac{dA}{dx} + \mu A + A^3 - A^5 = 0, \quad (21)$$

with the boundary conditions

$$A(0) = 0, \quad A(+\infty) = A_2. \quad (22)$$

If we replace U_0 by v , Eq. (21) becomes identical to Eq. (11) but with a different boundary condition. A nonlinear global mode is represented by a trajectory in phase space linking a point where $A(0) = 0$ with $dA/dx(0) \neq 0$ to A_2 . Graphically, the existence of global modes for the system can be deduced from the phase portraits (Fig. 2). For fixed parameters μ and U_0 , a global mode exists if the stable manifold of A_2 intersects the line $A = 0$ at a point different from A_0 . We shall notice that, in contrast with the selection problem faced when determining the front velocity as a function of μ , the problem is here the existence or nonexistence of a solution with respect to both control parameters U_0 and μ .

In the range $\mu_M < \mu < 0$, an NG mode exists only when $U_0 < v^{nl}(\mu)$ (light gray region in Fig. 3) as the orbit asymptotic to A_2 crosses at least one time the axis $A = 0$ with $dA/dx \neq 0$ (Fig. 2(c)). When $v_{n+1} < U_0 < v_n$, n intersection points exist corresponding to n different NG solutions. When $U_0 > v^{nl}(\mu)$ (white region in Fig. 3), no NG mode exists since the stable manifold of A_2 comes from A_1 (Fig. 2(a)).

In the range $0 < \mu < 3/4$, the stable manifold of A_2 crosses at least one time the axis $A = 0$ with $dA/dx \neq 0$ for $U_0 < v^{nl}(\mu)$ (Figs. 2(e) and (f)) and the number of intersections increases when approaching the curve $U_0 = v^1(\mu)$. In the domain $v^1(\mu) < U_0 < v^{nl}(\mu)$, a finite number of NG modes exist, as the orbit ending at A_2 connect to A_0 with a finite number of revolutions around A_0 (Fig. 2(e), medium gray region in Fig. 3). In the domain $0 < U_0 < v^1(\mu)$, an infinite discrete number of NG modes exists as the stable manifold of A_2 comes spiraling out from A_0 (Fig. 2(d), dark gray region in Fig. 3).

In the range $\mu > 3/4$, the orbit asymptotic to A_2 crosses $A = 0$ only for $U_0 < v^1(\mu)$ when the fixed point A_0 becomes an unstable focus (see Fig. 2(f)). In this case, an infinite number of global modes bifurcate at the same time (dark gray region in Fig. 3).

These results may also be expressed fixing U_0 and varying μ in which case a global mode exists when $\mu > \mu_A(U_0)$, where μ_A is defined by Eqs. (20a) and (20b). The number of NG modes is infinite above $\mu_A^1(U_0)$ (dark gray region in Fig. 3).

It is quite remarkable that the determination of the NA instability region based on the sign of the front velocities in an infinite domain coincides with the NG instability region in a semi-infinite domain. This allow us to propose a new criterion to determine the front velocity selection: The selected front may be viewed as the marginal global mode, i.e. the global mode with zero slope at the origin and, therefore, $v(\mu)$ is such that $\mu = \mu_A(v)$.

3.2. Existence of global modes and scaling laws

Whereas the front selection is based on a conjecture, the existence of a global mode can be demonstrated rigorously by matched asymptotic expansions corresponding to the perturbative arguments sketched in Figs. 4(a) and (c) for $U_0 < \sqrt{3}$ and Fig. 4(d) for $U_0 > \sqrt{3}$. When $U_0 < \sqrt{3}$, at the NG threshold, the stable manifold of A_2 connects with the most unstable manifold of A_0 . This solution is known [29] to be structurally unstable. This is shown in Fig. 4(c): the heteroclinic trajectory emanates from the most unstable eigendirection corresponding to the largest eigenvalue of Eq. (21) linearized around origin. A small change in the control parameter μ around the value μ_A perturbs this orbit which can no longer be tangent to the most unstable eigendirection. For $U_0 < 1/\sqrt{3}$, the other direction is stable and the perturbed trajectories are shown in Fig. 4(b). For $1/\sqrt{3} < U_0 < \sqrt{3}$, A_0 is an unstable node, the perturbed trajectory emanates from the least unstable eigendirection and, when $\mu > \mu_A$, it makes one about turn around the origin in order to connect with A_2 . It crosses the axis $A = 0$ at a point where $dA/dx \neq 0$, and corresponds to a global mode. When $U_0 > \sqrt{3}$, the particular solution existing at $\mu = \mu^{nl}(U_0)$ corresponds to an heteroclinic orbit tangent to the least unstable eigendirection at the origin which is structurally stable. Perturbation of this orbit through a variation of μ still leads to trajectories that remain tangent to the least unstable eigendirection (Fig. 4(e)). In such an instance, no NG mode is obtained.

In this section, we explicitly perturb the heteroclinic orbit prevailing at the bifurcation parameter $\mu = \mu_A(U_0)$ for a fixed advection velocity U_0 . We demonstrate that a global mode exists as soon as $\mu > \mu_A$ (with $\mu_A = \mu^{nl}(U_0)$ when $U_0 < \sqrt{3}$, and $\mu_A = \mu^l(U_0)$ when $U_0 > \sqrt{3}$). Details of the calculations can be found in Appendix B.1.

This allows us to establish scaling laws with respect to a departure from the nonlinear absolute instability threshold $\epsilon = \mu - \mu_A$ for the slope at the origin $dA/dx(0)$ and for the characteristic size of the initial growth region of the global mode defined as the distance at which $A = 0.99A_2$.

In the parameter range $U_0 < \sqrt{3}$, the nonlinear selection criterion for the front velocity is expected to apply; the absolute instability threshold $\mu_A = \mu^{nl}(U_0)$, and the shape of the front at this value of the bifurcation parameter are known analytically (see Appendix B.1). We determine the perturbed solutions in the following way: For $\mu = \mu_A + \epsilon$ with $\epsilon \ll 1$, the solutions of Eq. (21) with boundary conditions (22) are the functions with $u(A) = dA/dx$ which satisfy

$$u u' - U_0 u + \mu A + A^3 - A^5 = 0, \tag{23}$$

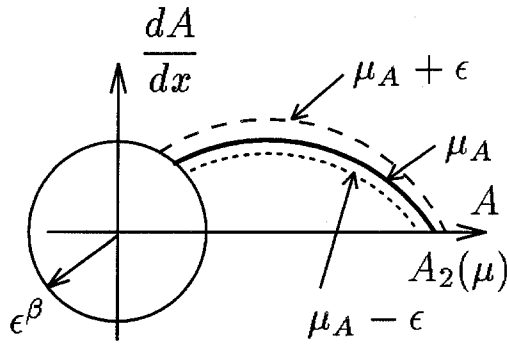
where the prime denotes differentiation with respect to A . Under this change of variable, the initially second-order equation (21) becomes first-order and the two boundary conditions (22) are transformed into

$$u'(A_0) = U_0, \quad u(A_2(\mu)) = 0. \tag{24}$$

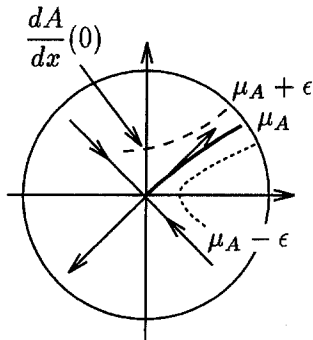
The first boundary condition $u'(A_0) = U_0$ results from writing (23) at $A = A_0$ and exploiting the original constraint $u(A_0) \neq 0$ on the existence of a global modes. One of the two boundary conditions has to be dropped in order to solve (23) and (24) in the singular limit $\epsilon \ll 1$ and an inner region of size ϵ^β has to be introduced in the neighborhood of the origin (see Figs. 4(a)–(c)). The inner solution satisfies the condition $u'(A_0) = U_0$ whereas the outer solution satisfies the condition $u(A_2(\mu)) = 0$. The method of matched asymptotic expansions [30] is applied and the matching of inner and outer solutions imposes the size of the inner region to be ϵ^β with

$$\beta = \frac{\sqrt{3} + U_0}{2(\sqrt{3} - U_0)}. \tag{25}$$

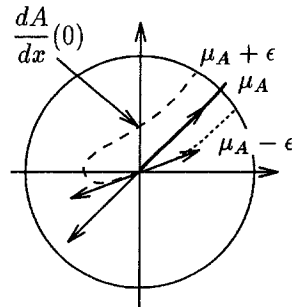
This result is valid for $\beta > 0$, i.e. $U_0 < \sqrt{3}$. When $U_0 > \sqrt{3}$, the inner solution does not cross the axis $A = 0$ and no NG mode exists for $\mu = \mu^{nl}(U_0) + \epsilon$, $\epsilon \ll 1$. In Fig. 4(e) one sees that when $U_0 > \sqrt{3}$, matching of the inner



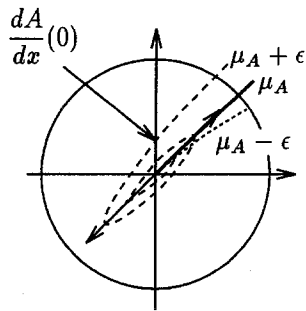
(a) Outer solution



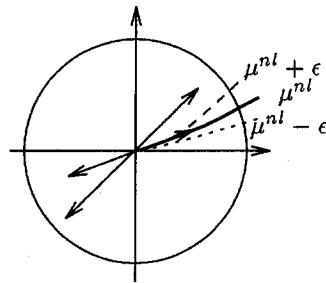
(b) A_0 saddle, $0 < U_0 < 1/\sqrt{3}$.



(c) A_0 unstable node, $1/\sqrt{3} < U_0 < \sqrt{3}$.



(d) A_0 unstable focus, $U_0 > \sqrt{3}$.



(e) A_0 unstable node, $U_0 > \sqrt{3}$, $\mu = \mu^{nl}$.

Fig. 4. Matching of inner and outer solutions. The solution drawn in continuous line is the basic solution at the nonlinear instability threshold. The solution drawn in dashed lines is the perturbed solution above μ_A . The dotted line represents the solution for μ smaller than μ_A .

and outer solutions is always possible but the inner solution remains tangent to the less unstable manifold at A_0 with no revolution around A_0 and never crosses the $A = 0$ axis. This confirms that the law for the global instability threshold μ_A changes as U_0 exceeds $\sqrt{3}$ since $\mu^{nl}(U_0)$ is no longer the threshold of NG instability when U_0 exceeds $\sqrt{3}$.

The slope $u(A_0)$ is given as a function of the departure ϵ from the absolute instability threshold by the expression

$$u(A_0) \simeq v_0 \epsilon^\beta, \quad (26)$$

where the constant v_0 is given by the matching (Eq. (B.19) of Appendix B.1).

The characteristic growth size of the global mode is defined as the distance Δx such that $A(\Delta x) = 0.99A_2$. It may be calculated by adding the x -thickness of the inner region and the size of the outer solution between the boundary of the inner layer ($A = \epsilon^\beta$) and the point at which the amplitude reaches the value $0.99A_2$. Details of the calculation are given in Appendix B.2. The scaling law so obtained is given by

$$\Delta x \simeq \frac{4}{\sqrt{3} + U_0} (-\beta \ln \epsilon + \ln K), \quad (27)$$

where the constant K is found by the matching (Eq. (B.26) of Appendix B.2). If U_0 is set to zero and only the dominant term is taken into account, the result of Couillet et al. [31] valid for $U_0 = 0$ is recovered.

In the parameter range $U_0 > \sqrt{3}$, the system simultaneously becomes NG and A unstable at the control parameter value $\mu^1 = U_0^2/4$. The solution of Eq. (23) with boundary conditions (24) is known analytically as a series whose coefficients have to be determined numerically (see Appendix C.1). Except for the fact that we are now dealing with an infinite series⁵ for the order zero external solution instead of a polynomial, the subsequent steps of the method are the same as in the previous case: for a bifurcation parameter setting $\mu = \mu^1 + \epsilon$, $\epsilon \ll 1$, Eq. (23) is solved subject to the boundary condition $u'(A_0) = U_0$ in the inner layer and the condition $u(A_2(\mu)) = 0$ in the outer layer (see Fig. 4(d)). The inner solution may be calculated explicitly; the outer solution takes the form of a numerically determined series. Matching of the two solutions again leads to the determination of the inner layer thickness, to the scaling laws for the slope of the solution at the origin $u(A_0)$ and for its growth size Δx , and to an additional solvability condition (Eq. (C.12) of Appendix C.1) which may be checked numerically. The scaling law for the slope at the origin is given by

$$u(A_0) \simeq v_0 \epsilon \exp\left(-\frac{U_0 \pi}{2\sqrt{\epsilon}}\right), \quad (28)$$

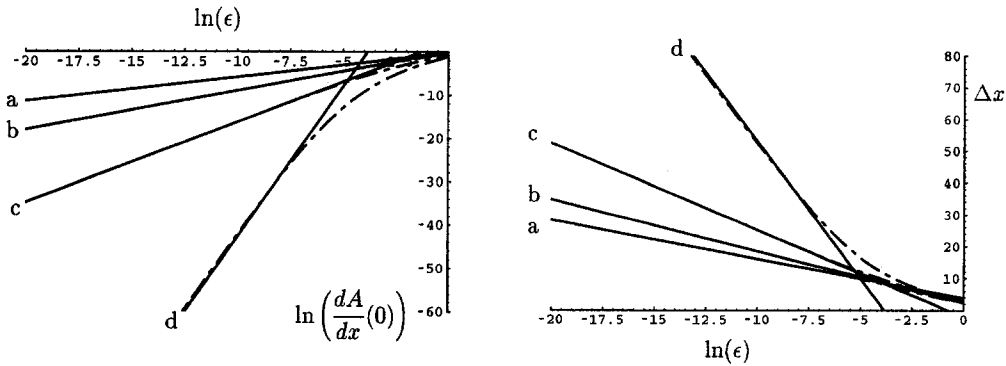
where the term v_0 represents the slope at the origin of the inner solution $d\xi/dx$ (ξ being the inner variable), as given in Eq. (C.14) of Appendix C.1. The growth size of the solution is given by

$$\Delta x \simeq \pi/\sqrt{\epsilon}. \quad (29)$$

The success of the matching procedure a posteriori proves that the NG instability threshold μ_A indeed follows the linear criterion when $U_0 > \sqrt{3}$. Numerically, we are able to perform the matching only for $U_0 > \sqrt{3}$ since for $U_0 < \sqrt{3}$, the additional solvability condition (Eq. (C.12) of Appendix C.1) cannot be fulfilled.

Each scaling law for the growth size of NG modes is characteristic of one kind of transition to an NG instability. Indeed, when the NG instability occurs while the system is convectively unstable ($U_0 < \sqrt{3}$), the growth size of NG modes scales as $\ln(1/\epsilon)$ (Eq. (27)), whereas it scales as $\epsilon^{-1/2}$ (Eq. (29)), when the NG instability occurs at the C/A transition ($U_0 > \sqrt{3}$).

⁵ Which should be numerically estimated in each case.



(a) $dA/dx(0)$ versus ϵ

(b) Characteristic growth size Δx of the nonlinear global modes

Fig. 5. Scaling laws for the subcritical model with $U_0 < \sqrt{3}$: (a) $U_0 = 0.1$, (b) $U_0 = 0.5$, (c) $U_0 = 1.0$, and (d) $U_0 = 1.5$. The dashed lines represent the numerical values. The continuous lines represent the theoretical values. In (a) and (b) numerical and theoretical values are almost identical.

The above scaling laws (26)–(29) have been validated by direct numerical integration of system (14a) and (14b). Numerical values of $u(A_0)$ and Δx for steady solutions are generated and compared with theoretical scaling predictions. The stable manifold of A_2 is obtained by backward variable step Runge–Kutta x -integration.⁶

The numerically computed value of $\ln(dA/dx(x = 0))$ are displayed in Fig. 5(a) as a function of the departure from criticality for four different advection velocities in the range $U_0 < \sqrt{3}$ ($U_0 = 0.1, 0.5, 1.0, 1.5$). The numerical values (dashed lines) of $\ln(dA/dx(x = 0))$ are in excellent agreement with theoretical predictions (continuous lines) for small U_0 . It can be seen that, as the advection velocity U_0 approaches $\sqrt{3}$, the domain of validity of scaling law (26) becomes restricted to a smaller neighborhood of the threshold μ^{nl} .

In order to validate scaling law (27) for the characteristic growth size Δx of global modes against the distance to the absolute instability threshold μ_A , all integration space steps between the amplitudes A_0 and $0.99 A_2$ were added together. Predicted values given by the theoretical scaling law (27) (continuous lines in Fig. 5(b)) are in very good agreement with their numerical counterparts (dashed lines) for small advection velocities. As U_0 approaches $\sqrt{3}$, the agreement is restricted to small ϵ .

Scaling laws (28) and (29) giving the slope of the global mode at the origin and its characteristic growing size in the range $U_0 > \sqrt{3}$ are checked numerically in the same way. Corresponding results are gathered in Fig. 6. We indeed verify that $\ln |\ln(dA/dx(x = 0))|$ and $\ln \Delta x$ are linear as functions of $\ln \epsilon$ as long as ϵ remains sufficiently small. For higher ϵ , theoretical results and numerical values diverge in Fig. 6(a) due to the contribution of higher-order terms in ϵ . As detailed in Appendix C.1, v_0 is given by a series which converges very slowly. However, we do verify in Fig. 6 that the series is adequately converged.

The solvability condition resulting from matching between inner and outer solutions takes the form

$$\sum_0^\infty w_k = 0 \quad \text{if } U_0 > \sqrt{3}, \quad \sum_0^\infty w_k \neq 0 \quad \text{otherwise,} \tag{30}$$

⁶ In order to validate the scaling laws completely, we have to check that the computed stable manifold of A_2 is indeed dynamically selected in a temporal simulation of (1). This will be done in Section 4.

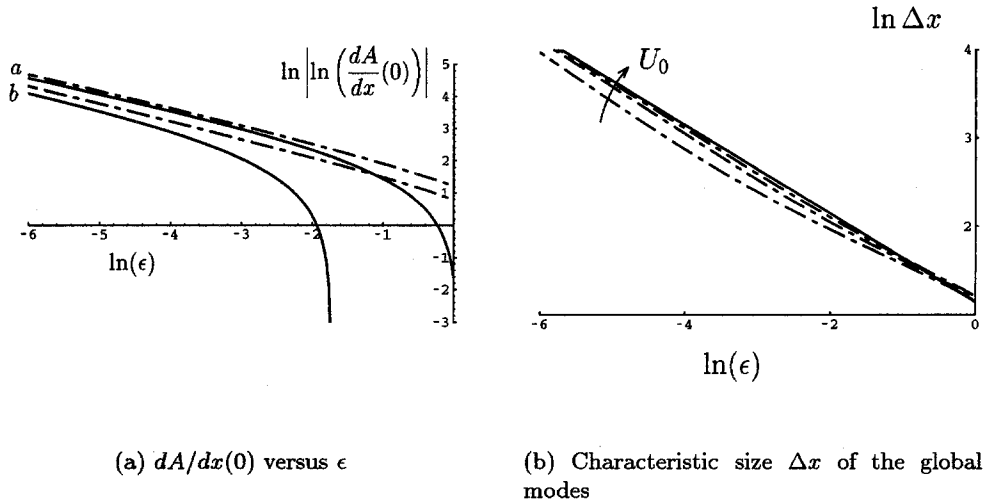


Fig. 6. Scaling laws for the subcritical model with $U_0 > \sqrt{3}$: (a) $U_0 = 3.0$ and (b) $U_0 = 2.0$. The dashed lines represent the numerical values. The continuous lines represent the theoretical values.

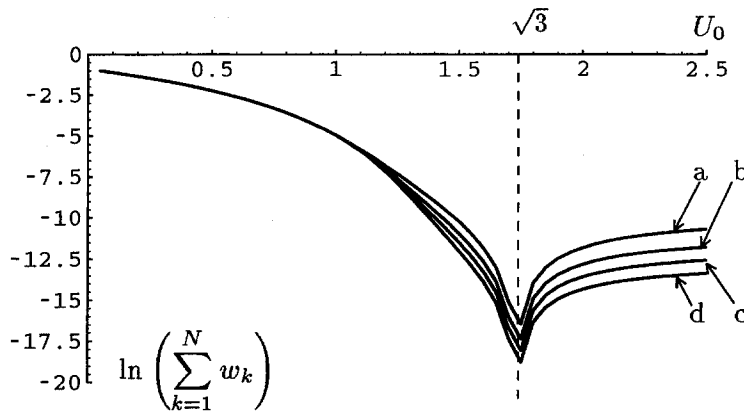


Fig. 7. Zero-order of the matching versus U_0 : (a) $N = 200$, (b) $N = 500$, (c) $N = 1000$, and (d) $N = 2000$.

where the numerically determined w_k depend on U_0 and $\mu_A(U_0)$ (see Appendix C.1). Fig. 7 indicates that $\sum_0^N w_k$ is different from zero for $U_0 < \sqrt{3}$ and zero for $U_0 > \sqrt{3}$. Note that e^{-15} nominally corresponds to zero in Fig. 7 as determined by numerical accuracy. The value of $\sum_0^N w_k$ approaches closer to zero for $U_0 > \sqrt{3}$ as the number of terms N in the series increases.

This result is important since it validates the linear criterion for the existence of nonlinear global modes in the region $U_0 > \sqrt{3}$, $\mu > U_0^2/4$. It also demonstrates that in the range $U_0 < \sqrt{3}$, the curve $\mu^1 = U_0^2/4$ does not signal the appearance of a nonlinear global mode since the matching cannot be done between an inner solution with $v_0 \neq 0$ and the series solution (C.2) at $\mu = \mu^1$. It is worth noting again that in the region $U_0 < \sqrt{3}$, $\mu < U_0^2/4$, a nonlinear global mode exists, despite the fact that the basic state is linearly convectively unstable or linearly stable.

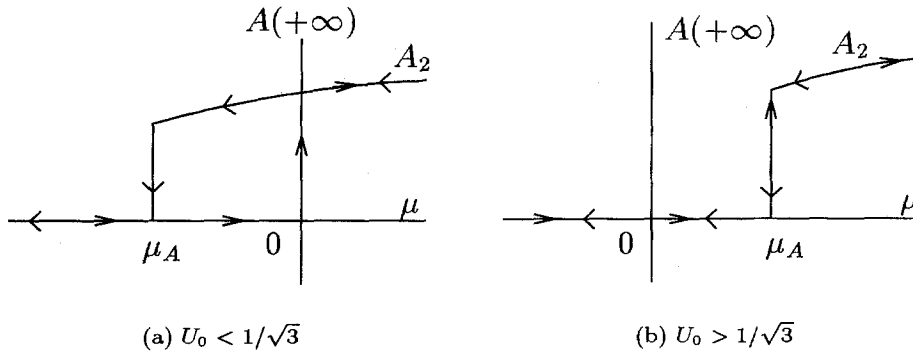


Fig. 8. Numerically obtained values of A at $x \rightarrow +\infty$ and $t \rightarrow +\infty$ versus the bifurcation parameter.

3.3. Hysteresis loop in the control parameter space

The study of global modes has allowed us to predict the nonlinear solutions of the system as a function of the control parameters μ and U_0 but not which one will be chosen. As pointed out by Chomaz [14], a hysteresis loop appears in the nonlinearly absolute range $\mu_A < \mu < 0$. The response of the system characterized by the amplitude at $x = +\infty$ (Fig. 8(a)) clearly shows the hysteresis loop between the unperturbed state and the NG mode. The hysteresis loop has been obtained numerically by computing the temporal solutions of partial differential equation (1) with potential density (2).

For $U_0 < \sqrt{3}$, let the system be in the initial uniform state A_0 . The parameter μ is then increased in a quasistatic manner while maintaining U_0 constant in the range $U_0 < 1/\sqrt{3}$ (see Fig. 8). As long as $\mu < \mu_A$, a single solution exists (A_0 everywhere). Above μ_A , a second global mode solution appears. In the absence of a large perturbation, the system is observed to remain in the uniform state A_0 until $\mu = 0$ because A_0 is linearly stable. Past $\mu = 0$, the uniform solution A_0 becomes linearly unstable, and the system tips over to the global mode which is now the unique stable solution. As μ is now decreased, the system remains on the global mode branch as long as $\mu > \mu_A$ and returns to the uniform state A_0 when the global mode solution disappears at $\mu = \mu_A$.

For $U_0 > 1/\sqrt{3}$, the hysteresis loop no longer exists. The transition between solutions takes place at $\mu = \mu_A$ now positive with no hysteresis but a jump in the value of $A(+\infty)$ from zero to its global mode value (see Fig. 8(b)).

3.4. Multiplicity of global modes

In the previous perturbative approach, we have not taken into account a possible multiplicity of global modes at given control parameter. In general, as mentioned in Section 3.1 there exist several solutions satisfying Eq. (21) and associated boundary conditions (22).

As seen from the phase portrait sketched in Fig. 9(a), the global mode multiplicity is related to the number of turns around the origin of the solution asymptotic to A_2 . As already explained in Section 3.1, when $\mu > \mu^1(U_0)$, the point A_0 is an unstable focus and there exists a discrete infinity of global modes linking the amplitude $A_0 = 0$ at $x = 0$ to A_2 at $x = +\infty$. In the domain of parameter space where the system is NG and C unstable (light and medium gray regions in Fig. 3), a finite number of global modes exist as the stable manifold of A_2 makes a finite number of turns around A_0 . This number increases when parameters are close to the curve $\mu = \mu^1(U_0)$.

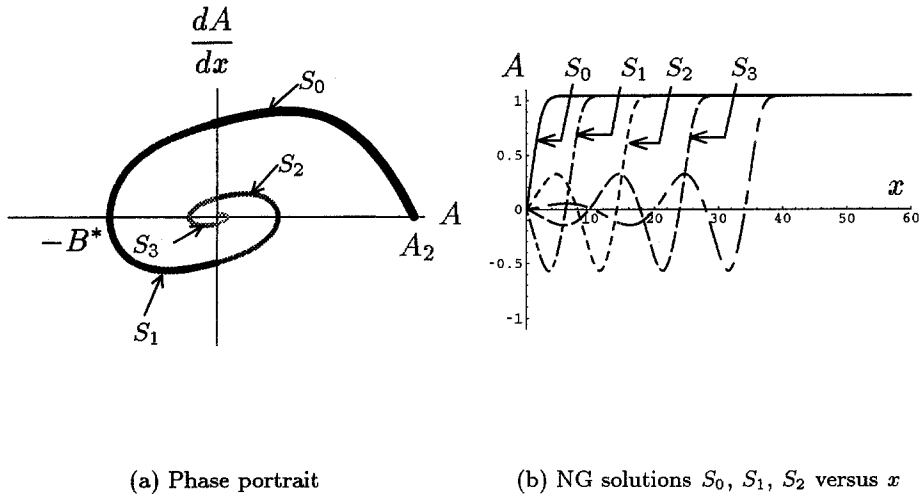


Fig. 9. Multiplicity of global modes ($\mu > 0$ in this figure). Only S_0 verifies Eq. (21) with boundary conditions (22) without oscillating around A_0 .

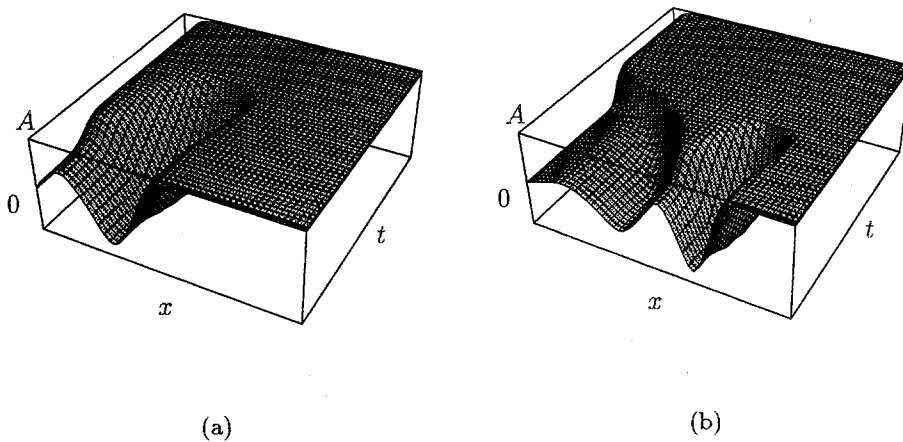


Fig. 10. (a) Simulation starting from the solution such that $A(0) = 0, A(+\infty) = A_2$ and crossing zero twice. $U_0 = 0.1, \mu = -0.01$. (b) Simulation starting from the solution crossing zero four times. $U_0 = 0.1, \mu = 0.001$.

The existence of a Lyapunov functional $\mathcal{L}(A)$ given by (10) trivially enables us to conclude that the steady solution with the smallest characteristic extent Δx , i.e. the solution with no oscillations around the origin, corresponds to the absolute minimum of $\mathcal{L}(A)$. However, the linear stability of the other solutions has to be determined.

We make the following conjecture, which has been numerically verified for a large set of temporal simulations: all the NG modes which oscillate around the origin before reaching A_2 are unstable. In other words, for fixed boundary conditions, the only stable steady solution is the one with the smallest characteristic extent Δx .

An example of temporal simulation is presented in Fig. 10(a). For $\mu = -0.01$ and $U_0 = 0.1$, the steady solution oscillating twice around the origin (S_2 in Fig. 9), obtained by numerical integration of Eq. (21) in the phase space with associated boundary conditions (22), is used as the initial state at $t = 0$ for the temporal simulation. The solution is seen to evolve to the stable trajectory linking A_0 to A_2 with no oscillation.

Similarly, an NG mode oscillating four times around A_0 freely evolves toward the NG mode with no oscillation in Fig. 10(b).

4. Signaling problems

In this section, we examine the response of the system to an external forcing at the origin. We therefore assume that the system is forced at a constant steady amplitude $A(0) = B$ at the origin (because of the symmetry $A \rightarrow -A$, B is assumed to be positive). We look for steady solutions of (1) with potential density (2). As in the case of global modes, the existence of a Lyapunov functional implies that A reaches an extremum of $\mathcal{V}(A)$ at $+\infty$, i.e. $A(+\infty) = A_0$ or A_2 . The procedure used to find these forced solutions is similar to the determination of NG modes. One may determine on the phase portraits (see Fig. 2) if the line $A = B$ intersects the stable manifold of either A_2 or A_0 . In order to clarify the description of the possible solutions in parameter space, the reader may refer to Fig. 11 which summarizes the results obtained in the various regions of the (μ, U_0) space discussed below.

In the gray regions, solutions with $A(+\infty) = A_2$ for $A(0) = B$ exist but only for $B \neq 0$. In the light gray region, infinitely small B are sufficient whereas in the two darker gray zones, forcing has to exceed a threshold amplitude to obtain $A(+\infty) = A_2$. In the darkest gray region, the threshold is different if the forcing is increased or decreased.

In the NG region ($\mu > \mu_A(U_0)$), when the NG mode is triggered once, the system cannot relax back to A_0 even if the forcing is removed. This behavior reflects the intrinsic response of the system. In the NC region (gray regions with $\mu > \mu_M$), the system follows the variations of the forcing and returns back to A_0 when the forcing is removed (with hysteresis cycle in the dark gray region).

This nonlinear spatial amplifier behavior was expected in the NC region, but it surprisingly persists in the NS region when $\mu > \mu_s(U_0)$ (gray regions with $\mu < \mu_M$). The system relaxes toward A_0 for any forcing, only if $\mu < \mu_s(U_0)$. As a conclusion, the region of parameter space where the system acts as a nonlinear spatial amplifier contains not only the NC region but also part of the NS region. NC instability is only a sufficient condition to obtain a saturated response at infinity in the signaling problem.

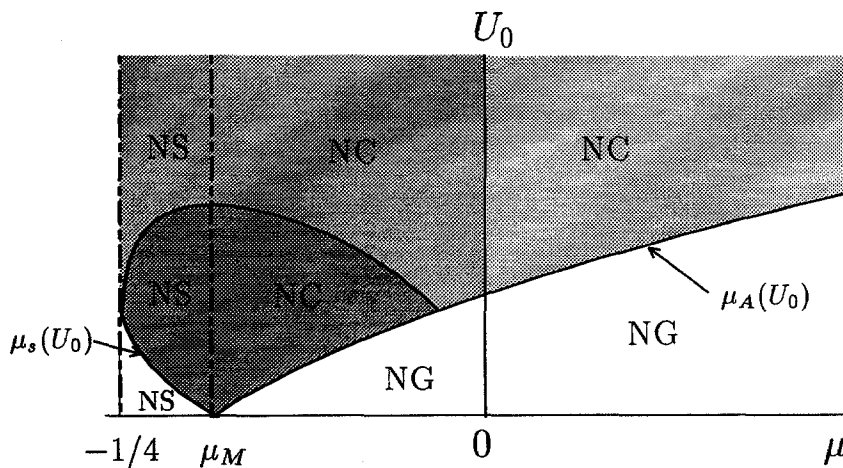
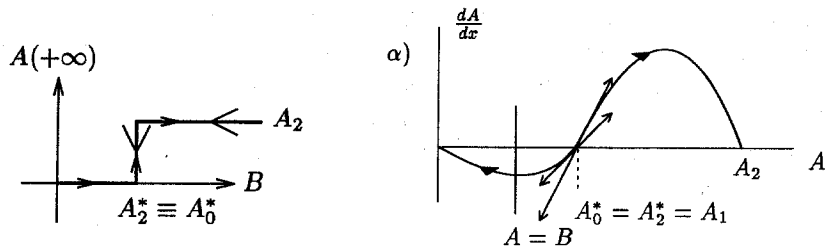


Fig. 11. Regions of nonlinear global (NG) instability in the parameter space (white and $\mu > \mu_M$) and of NC instability (gray and $\mu > \mu_M$). The system acts as a nonlinear spatial amplifier in the gray regions. In the dark gray region, A_1 is an unstable spiral (Appendix A) and hysteretic behavior is obtained. In the medium gray region, forcing must exceed a critical threshold to be efficient. In the light gray region, even small forcing amplitudes are amplified. The nonlinearly stable (NS) region ($\mu < \mu_M$) contains a subdomain (gray) where the physical behavior of the system with respect to forcing is identical to the one in the NC region.

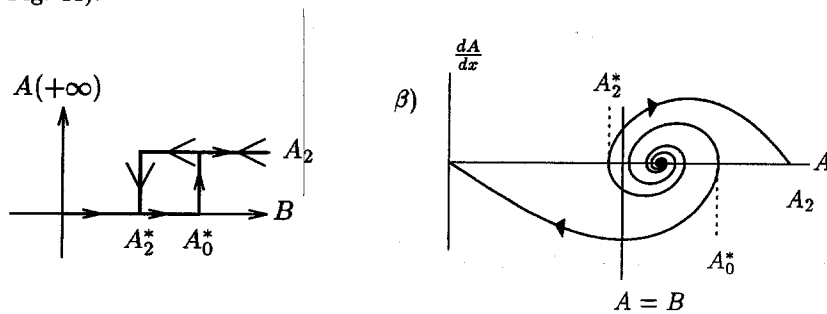
4.1. Response to a forcing in the nonlinearly convective instability region

4.1.1. Evaluation of the hysteresis loop with the forcing parameter

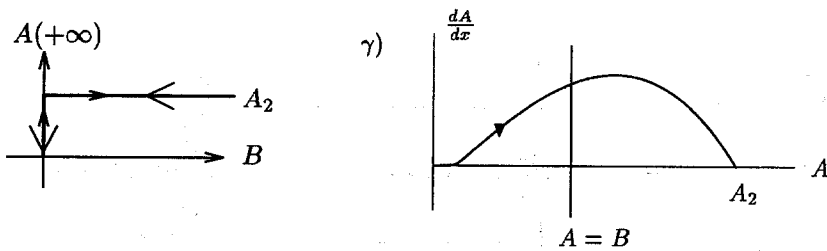
When $\mu > 0$, A_0 is an unstable node (see Appendix A). Therefore, whatever μ and $B \neq 0$, the forced solution $A(0) = B$ will end up in A_2 and no hysteresis is possible (Fig. 12(c)). When $\mu < 0$, the stable manifold of A_2 possesses a point of minimum amplitude A_2^* (Figs. 12(a) and (b)). A solution asymptotic to A_2 therefore exists if $B > A_2^*$ (see Figs. 12(α) and (β)). The stable manifold of A_0 possesses a maximum amplitude A_0^* . Therefore, at least one solution asymptotic to A_0 exists for a forcing amplitude $B < A_0^*$.



(a) $\mu_M < \mu < 0$ and A_1 is an unstable node (medium gray region on Fig. 11).



(b) $\mu_M < \mu < 0$ and A_1 is an unstable spiral (dark gray region of Fig. 11).



(c) $\mu > 0$ (light gray region of Fig. 11).

Fig. 12. Response of the system versus the forcing parameter in the NC domain and the phase space corresponding to each case.

When A_1 is an unstable spiral point (Fig. 12(β)) (see Appendix A), we have $A_2^* < A_1 < A_0^*$. Two solutions coexist for a forcing amplitude $A_2^* < B < A_0^*$: one relaxing toward A_0 , the other toward A_2 . When A_1 is an unstable node, we may have $A_2^* < A_1 < A_0^*$, but for high advection velocities, we have $A_2^* = A_1 = A_0^*$ and no multiple solution region exists (Fig. 12(α)).

In order to check numerically for hysteretic behavior with respect to forcing amplitude, we follow a procedure similar to that of Section 3.3: The system is initially set to the uniform state A_0 and integrated in time while μ is kept fixed and the forcing is gradually increased from $B = 0$ in a quasistatic manner.

The system presents the response measured at $x = +\infty$ depicted in Figs. 12(a) and (b): For $\mu < 0$ in the dark gray region in Fig. 11, when the forcing parameter B remains below the threshold A_0^* , the system is locked to the solution asymptotic to A_0 . When B exceeds A_0^* , the system tips over to the solution asymptotic to A_2 and remains locked to it as long as the forcing amplitude is kept above the lower threshold A_2^* .

The results of our numerical simulations are represented in Fig. 13 in order to illustrate this hysteretic behavior under forcing prevailing in the NC region when $\mu < 0$; initially, the solution is A_0 everywhere and B is increased quasistatically. In Fig. 13(a), the system travels along the lower branch of the hysteresis loop displayed in Fig. 12(b); in Fig. 13(b), it follows the upper branch. We indeed verify that the system tips over at the low and high threshold values A_0^* and A_2^* and therefore presents a clear hysteretic behavior to forcing.

4.1.2. Scaling law

A scaling law can be obtained for the minimum forcing amplitude A_2^* required to generate the bifurcated state A_2 at $x = +\infty$. The procedure is similar to the one followed for the determination of the scaling law for $dA/dx(x = 0)$ outlined in Section 3.2. If $\epsilon = \mu^{nl} - \mu$ denotes the distance to the NG instability threshold, the corresponding scaling law reads (Appendix B.1)

$$A_2^* \simeq C^* \epsilon^\beta, \tag{31}$$

where

$$C^* = A_2(\mu_A)^{1-3\beta}(\beta - 1)^{\beta-1} \left(\frac{\sqrt{3}}{2} B \left(\frac{1}{2\beta}; 2 - \frac{1}{2\beta} \right) \right)^\beta, \tag{32}$$

β is the previously introduced constant (Eq. (25)) and B denotes the beta function [32].

The response of the system *in the NC region for $\mu > 0$* as a function of forcing amplitude is represented in Fig. 12(c). Either $B > 0$ and the system is locked to the mode asymptotic to A_2 , or $B = 0$ and the system is

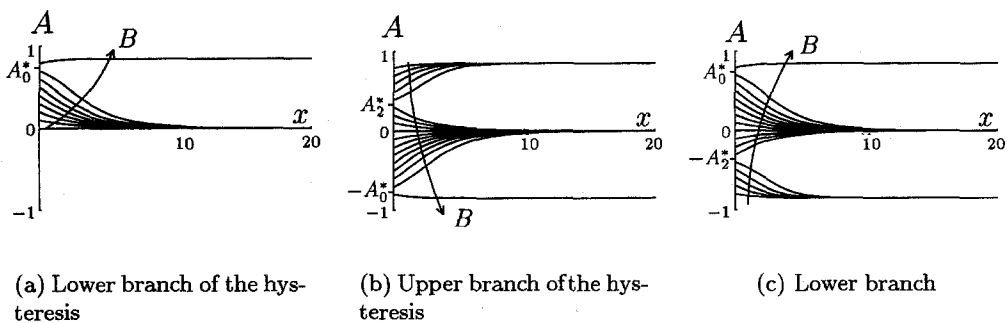


Fig. 13. Asymptotic response ($t \rightarrow \infty$) of the system versus the forcing parameter. Convective region $\mu < 0$.

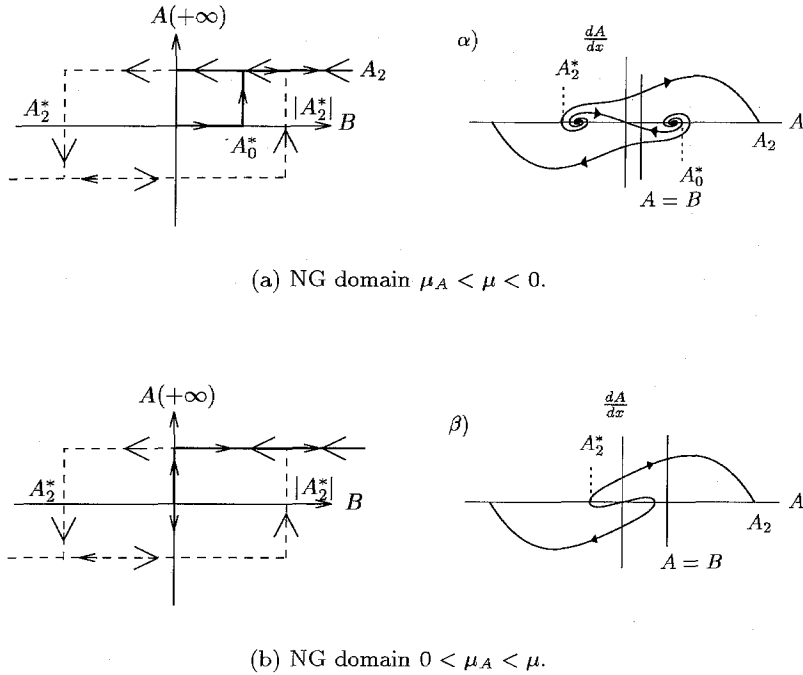


Fig. 14. Response of the system as a function of the forcing parameter and the corresponding solutions in the phase space (α), (β).

locked to the trivial solution $A = 0$ for all x . The system does return to the uniform state A_0 , as the forcing is suppressed.

4.2. Response to a forcing in the NG region

A forced solution asymptotic to A_2 exists for all B (even $B = 0$) in the NG region since the line $A = B$ always intersects the stable manifold of A_2 (Figs. 14(α) and (β)). This solution is obtained continuously from the global mode defined in Section 3 ($B = 0$) by shifting the origin to x_0 such that the amplitude of the NG mode at x_0 equals B . This weak effect of a forcing is in accordance with the fact that the NG mode may be interpreted as the intrinsic response of the system.

4.2.1. In the NG region for $\mu < 0$

In this region, forcing has an irreversible effect. If the system is initially set to the uniform state A_0 and the forcing is gradually increased from $B = 0$ in a quasistatic manner, the following sequence is obtained: the system keeps converging to A_0 at $x = +\infty$ until $B = A_0^*$ where it flips irreversibly to the NG branch (Fig. 15(a)). This first branch is similar to the first magnetization branch of ferromagnets. Then, even if B returns to zero, the system remains locked to A_2 . It is not possible to unlock it by removing the forcing (Figs. 14(a) and 15(b)). The system remains locked to the global mode asymptotic to A_2 for all B .

If one allows B to change sign, the system tips over to the global mode such that $A(+\infty) = -A_2$ for $B = A_2^*$ (negative in the NG region), and remains locked to this mode as long as $B < |A_2^*|$. A hysteresis loop is therefore possible (dashed lines in Figs. 14(a), 15(b) and (c)) but the system never relaxes to the solution asymptotic to A_0 .

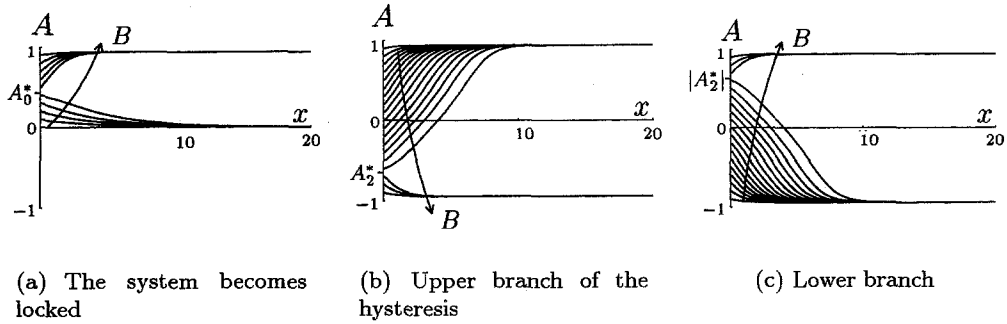


Fig. 15. Asymptotic response ($t \rightarrow \infty$) of the system versus the forcing parameter. NG region $\mu < 0$.

4.2.2. In the NG region for $\mu > 0$

In the NG region for $\mu > 0$ (gray region in Fig. 11), the solution asymptotic to A_0 no longer exists (Fig. 14(β)). Therefore, the behavior of the system is similar to the case $\mu < 0$ in the NG region but the branch which locks the system on the solution asymptotic to A_2 coincides with the axis $B = 0$ (Fig. 14(b)).

By contrast with the NC region, in the whole NG region, a nontrivial intrinsic response obtained by forcing the system remains even when the forcing is suppressed. The system never relaxes back to A_0 when the forcing is removed. This behavior is in accordance with the interpretation of global modes as the intrinsic response of the system.

4.3. Response to a forcing in the NS region

In the NS region $\mu < \mu_M$, the stable manifold of A_2 possesses the same features as in the NC region for $\mu_M < \mu < 0$: either its minimum amplitude A_2^* is merged into A_1 (as in Fig. 12(α)) or $A_2^* < A_1$ (this happens if A_1 is a spiral; see Fig. 12(β)).

The stable manifold of A_0 may also possess the same features as in the NC region, i.e. its maximum amplitude A_0^* is either merged into A_1 (Fig. 12(α)) or $A_0^* > A_1$ (Fig. 12($\beta\mu < \mu_M$) where the stable manifold of A_0 possesses no maximum amplitude. This region is limited by a line

$$\mu = \mu_s(U_0) \equiv \begin{cases} \frac{\mu_M}{3}(4 - (1 - \sqrt{3}U_0)^2) & \text{if } U_0 < \frac{1}{\sqrt{3}}, \\ -\frac{1}{4} & \text{otherwise,} \end{cases} \quad (33)$$

on which a heteroclinic orbit links A_2 to A_0 in the phase space (with $dA/dx < 0$). Note that such an orbit always exists for $\mu = -1/4$ if $U_0 > 1/\sqrt{3}$, since A_2 and A_1 merge one into another (saddle–node bifurcation).

In consequence, the response of the system in the NS region is the same as in the NC region if $\mu > \mu_s(U_0)$ and corresponds to Fig. 12(a) if A_1 is a node or to Fig. 12(b) if A_1 is a spiral. But if $\mu < \mu_s(U_0)$, the system cannot be forced regardless of the forcing amplitude and always relaxes back to A_0 .

5. Genericity

In order to test the genericity of the previous scenarios, we successively examine a supercritical bifurcating mode, a van der Pol–Duffing-like model, and a transcritical model. They all leave $A_0 = 0$ as a solution of the system. In the

three cases, the formulation is chosen so that the linear absolute transition remains at the value $\mu^1(U_0) = U_0^2/4$. In particular, we wish to demonstrate that linear absolute instability is only a sufficient condition for nonlinear global instability and that, even in the case of a supercritical bifurcation, the system may be nonlinearly globally unstable while being locally convectively unstable.

5.1. Supercritical bifurcation

In the case of a supercritical bifurcation, the potential density is taken to be

$$\mathcal{V}(A) = -\mu A^2/2 + A^4/4 \tag{34}$$

and the classical bifurcation diagram involves the basic state $A_0 = 0$ and the bifurcated state $A_2(\mu) = \sqrt{\mu}$. Upon substituting the expression for the potential density in Eq. (1), we obtain

$$\frac{\partial A}{\partial t} + U_0 \frac{\partial A}{\partial x} = \frac{\partial^2 A}{\partial x^2} + \mu A - A^3. \tag{35}$$

Note that the parameter U_0 is superfluous because the change of scale ($x \rightarrow x/U_0, t \rightarrow t/U_0^2, A \rightarrow U_0 A, \mu \rightarrow U_0^2 \mu$) rescales it to unity. Nevertheless, we keep it in the equation in order to draw a parallel with our previous study. In the supercritical case, there exists no domain of parameter space where the system becomes NG unstable while C unstable (see Fig. 16). The phase portraits of steady solutions of (35) are strictly analogous to those pertaining to the density potential (2) when $U_0 > \sqrt{3}$.

In the range $\mu < \mu^1(U_0)$, the phase portraits are of type Fig. 17(a) while for $\mu > \mu^1(U_0)$ they are of type Fig. 17(b). The curve $\mu = \mu^1(U_0)$ signals a change in local behavior of the trajectories around A_0 (between an unstable node for $\mu < \mu^1$ and an unstable focus for $\mu > \mu^1$). It also coincides with the transition to NG instability.

Using matched asymptotic expansions, it is possible to show that the stable manifold of A_2 crosses the $A = 0$ axis with $dA/dx \neq 0$ only when $\mu > \mu^1$ (Appendix D). It is also possible to determine the scaling law for $dA/dx(x = 0)$ as a function of the distance to the NA instability threshold, as has been done in the case of a subcritical bifurcation with $U_0 > \sqrt{3}$. Details of the calculation are given in Appendix D. The final result is

$$\frac{dA}{dx}(0) \simeq v(0)\epsilon \exp\left(-\frac{U_0\pi}{2\sqrt{\epsilon}}\right) \tag{36}$$

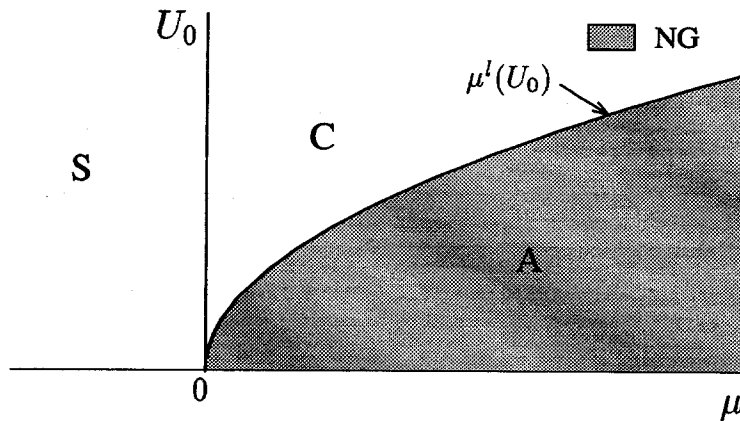


Fig. 16. Parameter space for the supercritical model. NG modes exist in the gray region which corresponds to the region of linear absolute instability for this model.

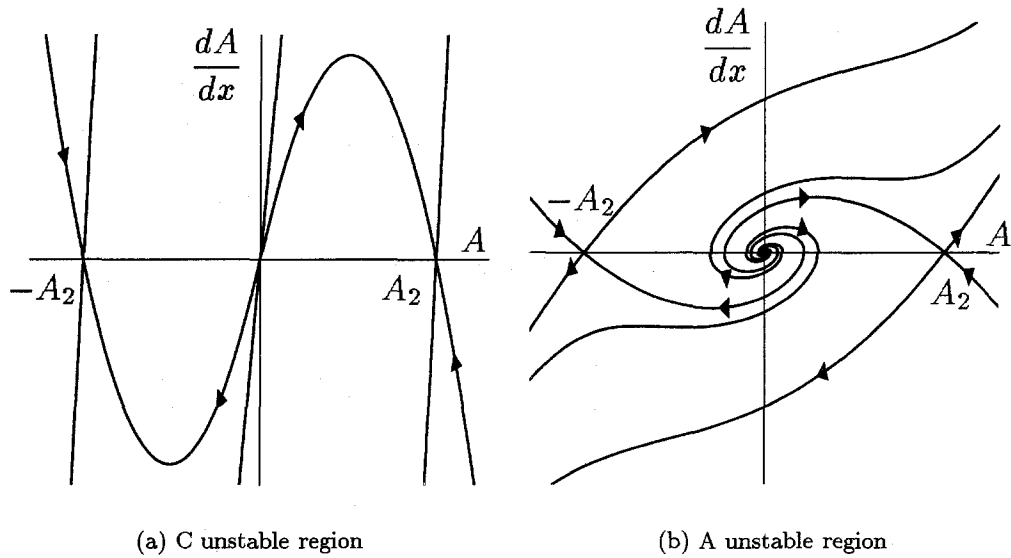
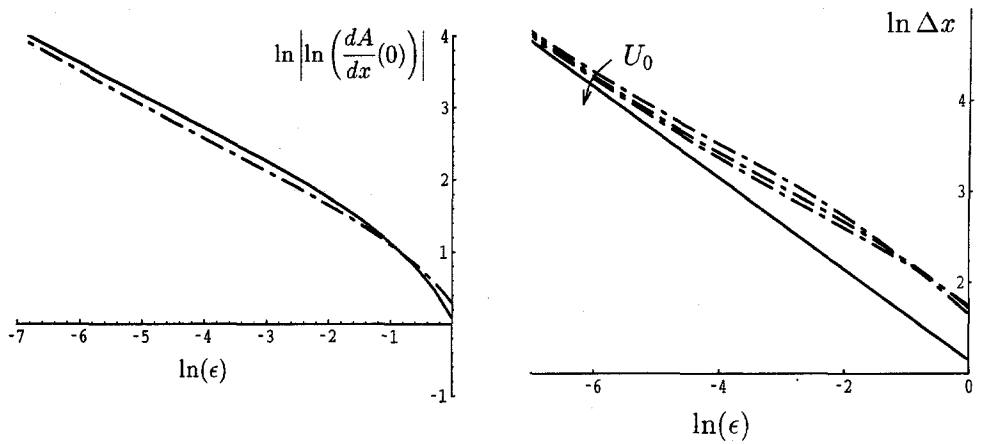


Fig. 17. Phase portraits of the supercritical model.



(a) $dA/dx(0)$ versus ϵ ; $U_0 = 1.0$.

(b) Characteristic growth size Δx of the global modes; $U_0 = 1.0, U_0 = 1.5, U_0 = 2.0$

Fig. 18. Scaling laws for the supercritical model. The dashed lines represent the numerical values. The continuous lines represent the theoretical values.

with the slope of the inner solution $v(0) \equiv d\xi/dx$ given by Eq. (D.5) of Appendix D (ξ is the inner variable). The characteristic growth size of the solution is given by

$$\Delta x \simeq \frac{\pi}{\sqrt{\epsilon}}. \tag{37}$$

Fig. 18 represents the comparison of the theoretical scaling laws (36) and (37) with the numerically obtained values of $\ln(dA/dx(x = 0))$ and Δx . For μ close to μ_A , we compute the global mode solution by backward integration

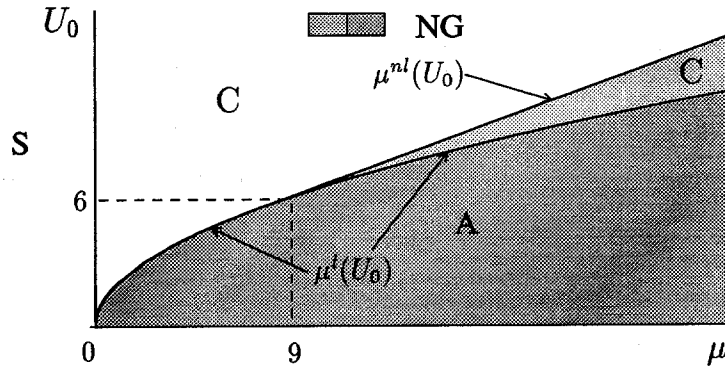


Fig. 19. Parameter space for the van der Pol–Duffing model. NG modes exist not only in the region of A instability but also in the region of C instability.

of the system (14a) and (14b) with potential (34) in order to find the stable manifold of A_2 . The predictions that $\ln |\ln(dA/dx(x = 0))|$ and $\ln \Delta x$ are linear versus $\ln \epsilon$ for the small values of ϵ are well verified.

In phase space $(A, dA/dx)$, a particular trajectory $u(A) = -(1/\sqrt{2})A(A - A_2)$ joining A_0 at $x = -\infty$ to A_2 at $x = +\infty$ exists for the specific value $\mu = 2U_0^2/9$. As in the case of the subcritical bifurcation for $U_0 > \sqrt{3}$, this solution does not correspond to a change of nature of the instability. The slope at the origin $\sqrt{\mu/2} = U_0/3$ of this particular solution is actually the smallest eigenvalue at $A = A_0$, whereas the largest eigenvalue is $2U_0/3$. As shown in Fig. 4(e), a perturbation of this particular solution remains tangent to the eigenvector with the smallest eigenvalue without taking negative values.

5.2. “Van der Pol–Duffing” model

In this section, we add a nonlinear term $A^2 \partial A / \partial x$ to Eq. (35). The amplitude equation is thus given by the two-parameter family known as the van der Pol–Duffing model

$$\frac{\partial A}{\partial t} + (U_0 - A^2) \frac{\partial A}{\partial x} = \frac{\partial^2 A}{\partial x^2} + \mu A - A^3. \tag{38}$$

The search procedure for particular steady solutions of Eq. (38) is carried out in the same way as before: we seek a polynomial solution $u(A)$ asymptotic to $A_2 = \sqrt{\mu}$ at $x = +\infty$ and to A_0 at $x = -\infty$ satisfying

$$uu' - (U_0 - A^2)u + \mu A - A^3 = 0. \tag{39}$$

This imposes $\mu = \mu^{nl}(U_0) \equiv 3(U_0 - 3)$, the solution being

$$u(A) = -\frac{1}{3}A(A^2 - A_2^2). \tag{40}$$

The straight line $\mu = \mu^{nl}(U_0)$ is tangent to the linear transition curve $\mu^1(U_0) = U_0^2/4$ for the parameters $\mu = 9, U_0 = 6$ (see Fig. 19).

The heteroclinic orbit linking A_2 from A_0 comes out therefore from the eigendirection⁷ corresponding to the smallest eigenvalue when $\mu < 9$, whereas its outgoing direction corresponds to the highest eigenvalue if $\mu > 9$. Therefore, an NG mode exists when $\mu > \mu^{nl}(U_0)$ for $\mu > 9$, whereas an NG mode exists only when $\mu > \mu^1(U_0)$

⁷ The slope at the origin of solution (40) is $A_2^2/3 = \mu^{nl}/3$ and the linear eigenvalues pertaining to Eq. (39) at $A = A_0$ are $\mu/3$ and 3 for $\mu = \mu^{nl}(U_0)$.

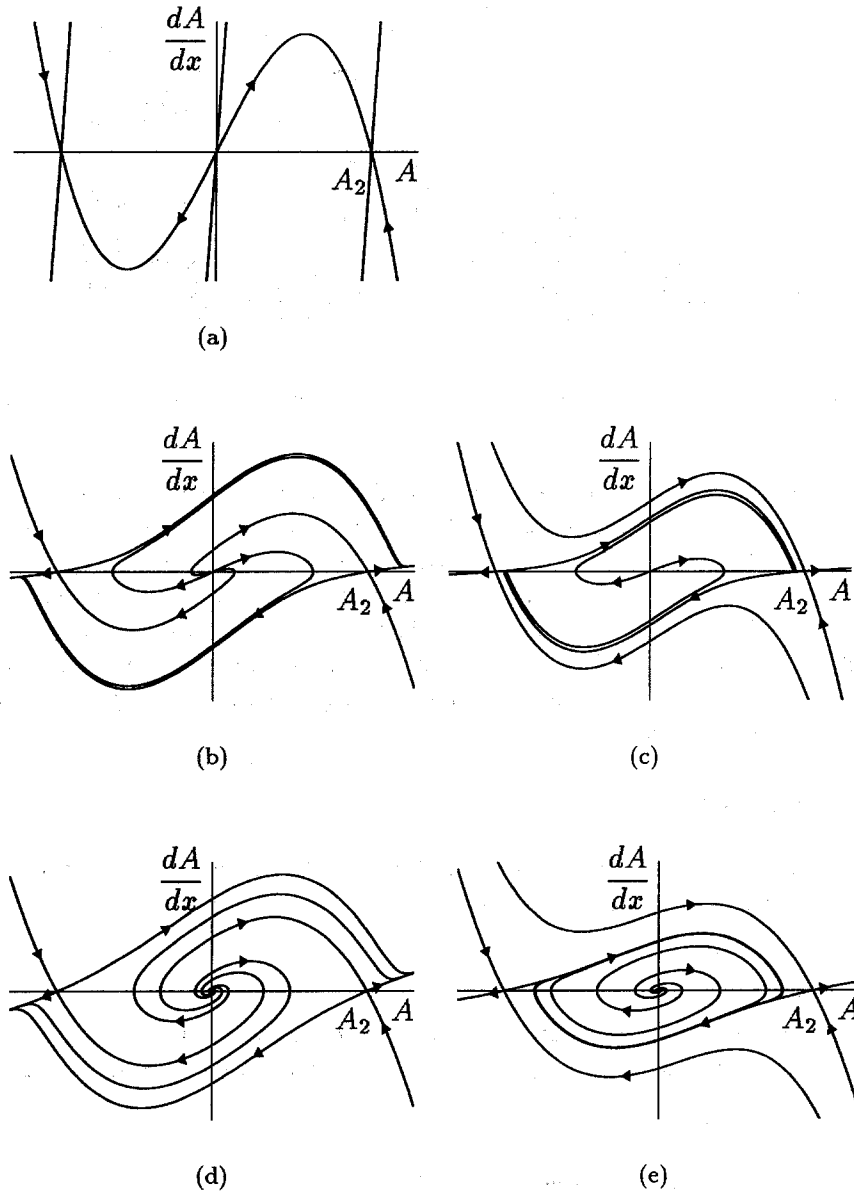


Fig. 20. Phase portraits of the van der Pol–Duffing model. (a): white C region in Fig. 19; (b) and (c): light gray C region; (d) and (e): dark gray A region. Phase portraits (c) and (e) are obtained for smaller advection velocities than (b) and (d), and display a limit cycle oscillation which do not alter the existence of NG modes.

for $\mu < 9$. The numerically obtained phase portraits are shown in the Figs. 20(a)–(e). In Figs. 20(a) and (e), the limit cycle of the van der Pol oscillator prevents the unstable manifold of A_0 from reaching A_2 . However, these phase portraits, and the existence of the limit cycle, are obtained for a bifurcation parameter in the NG unstable region (gray region) in Fig. 19 far above the NG instability threshold. Therefore, an NG mode still exists and its nature is not changed since it links a point of the $A = 0$ axis with $dA/dx \neq 0$ to A_2 . At the NG threshold, the birth

of the NG mode remains due to the presence of a heteroclinic trajectory linking A_0 to A_2 , and the limit cycle does not exist.

For $\mu > 9$, the system becomes thus NG unstable in a region where it is C unstable. The existence of NG modes could also be demonstrated by a matched asymptotic expansion for $\mu > \mu^{nl}(U_0)$ when $\mu < 9$ and $\mu > \mu^{nl}(U_0)$ when $\mu > 9$.

5.3. Transcritical bifurcation

In the present section we examine the case of a supercritical bifurcation perturbed by a cubic term breaking the symmetry $A \rightarrow -A$ in the potential. We keep the restabilizing order-4 term so that our model can be viewed as a perturbed supercritical case. This last model is similar to the model used by Ben-Jacob et al. [17] and Hakim [33] to illustrate the selection between linear and nonlinear front velocity. We choose the potential

$$\mathcal{V}(A) = -\mu \frac{A^2}{2} - \frac{A^3}{3} + \frac{A^4}{4}, \tag{41}$$

which, upon substitution into Eq. (1), yields

$$\frac{\partial A}{\partial t} + U_0 \frac{\partial A}{\partial x} = \frac{\partial^2 A}{\partial x^2} + \mu A + A^2 - A^3, \tag{42}$$

where μ and U_0 are the two control parameters as in the previous examples. The homogeneous steady solutions are $A_0 = 0$ for all μ and $A_1 = 1/2 - (\mu + 1/4)^{1/2}$ and $A_2 = 1/2 + (\mu + 1/4)^{1/2}$ for $\mu > -1/4$.

A steady particular solution of Eq. (42) linking the point A_0 to A_2 is sought as a polynomial function $u(A)$ which solves the equation

$$uu' - U_0 u + \mu A + A^2 - A^3 = 0. \tag{43}$$

This imposes $\mu = \mu^{nl}(U_0) \equiv -1/4 + (1/6 + \sqrt{2}U_0/3)^2$ (see Fig. 21). The corresponding solution reads

$$u(A) = -\frac{1}{\sqrt{2}}A^2 + \frac{U_0 + \sqrt{2}}{3}A \tag{44}$$

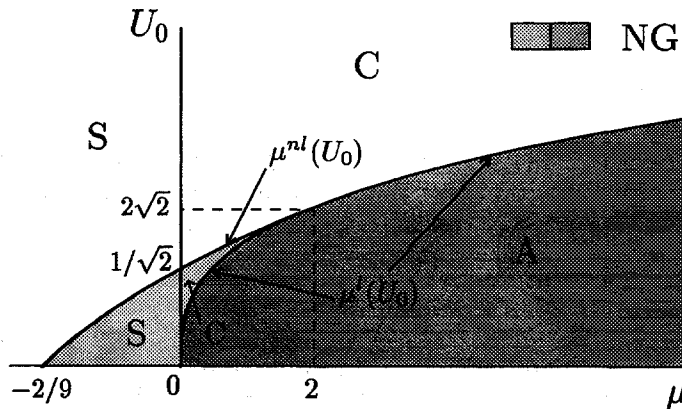


Fig. 21. Parameter space for the transcritical model.

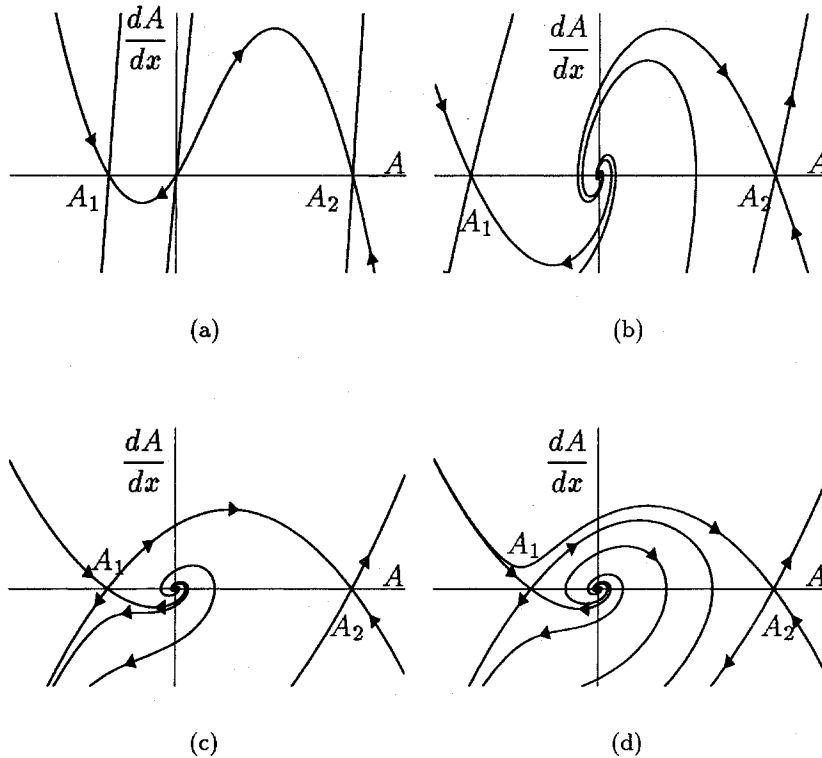


Fig. 22. Phase portraits of the transcritical model. (a) corresponds to the white C region in Fig. 21 whereas (b)–(d) correspond to the dark gray A region. Phase portraits similar to (b), (c) and (d) with a node behavior around the origin are obtained in the light gray C region.

and represents the heteroclinic orbit^{8,9} linking $A = A_0$ at $x = -\infty$ to $A = A_2$ at $x = +\infty$. The polynomial solution (44) originates from the eigendirection corresponding to the largest eigenvalue for $\mu < 2$ and to the smallest eigenvalue for $\mu > 2$. As in the previous case a global mode exists in the parameter space where $0 < \mu < 2$ and $U_0^1(\mu) < U_0 < U_0^{\text{nl}}(\mu)$. We verify with phase portrait Fig. 22(b) that the system is NG unstable in this domain. For $\mu > 2$, the NG and A instability thresholds coincide.

6. Conclusion

First we have identified, using published results, the NC/NA nature of the instability as a function of the advection velocity and the control parameter of the subcritical Ginzburg–Landau model. This determination only relies on the front velocity of a bifurcating state invading a basic state, the selection of which has been the object of recent studies.

⁸ This solution admits a slope at the origin $(U_0 + \sqrt{2})/3 = (1/2 + (\mu + 1/4)^{1/2})/\sqrt{2}$ which has to be compared with the eigenvalues of Eq. (43) linearized at $A = A_0$: $-1/\sqrt{2} - \sqrt{2}(\mu + 1/4)^{1/2}$ and $(1/2 + (\mu + 1/4)^{1/2})/\sqrt{2}$.

⁹ Another polynomial solution exists for $U_0 = 1/\sqrt{2}$ and for all $\mu > 0$: $u(A) = -(A^2 - A - \mu)/\sqrt{2}$ actually represents a heteroclinic orbit linking $A = A_2$ from $A = A_1$. This orbit brings no information as it is just a nonlinear global mode linking A_2 from $A = 0$ but $dA/dx \neq 0$ in a semi-infinite domain.

The NA/NC definition based on the existence and selection of a front in an infinite domain is somehow formal as the laboratory is artificially singled out. For this reason, we next considered NG instability in a semi-infinite homogeneous domain with zero-amplitude upstream boundary condition. This NG instability corresponds to the existence of a nontrivial nonlinear steady solution for which the direction of the advection has now to be considered as an eigendirection. The NG instability has been determined for the subcritical Ginzburg–Landau model and for three other variations on this theme: the supercritical Ginzburg–Landau model, the “van der Pol–Duffing” model, and the transcritical model.

For these cases that are homogeneous everywhere except at the origin, the domain of existence of an NG mode is rigorously determined from matched asymptotic expansions, and is shown to coincide with the NA region determined from front velocity selection consideration. As predicted from the conjecture that a nonlinear front at least propagates at the linear front velocity, the NG instability (or equivalently here the NA) domain totally overlaps the A region. Thus, A instability is only a sufficient condition for NG instability and cases where the system is simultaneously S or C and NG unstable have been exhibited.

Studying the signaling problem, i.e. the effect of adding a steady forcing at the origin, allows us to show how the NC and NA instability manifests itself by a particular behavior. We have shown that once triggered, the NG mode sustains itself forever and therefore represents the intrinsic behavior of the system in the NG region. On the contrary, a study of the signaling problem in the NC region demonstrates that the flow behaves as a nonlinear spatial amplifier of the incoming perturbation, exhibiting hysteretic behavior in some cases, but returning to zero when the forcing is removed. Surprisingly, the same behavior is observed in the NS region too. In this subcritical system, the advection associated with a strong forcing at the origin is able to lock on to a bifurcated solution. Therefore NC instability is only a sufficient condition for the flow to behave as a nonlinear spatial amplifier.

The absolute or convective nature of a flow may be experimentally determined by investigating the response of the system to a forcing at the origin. It seems to us that an experimental quantitative confirmation of the theory could be made for example by adding a mean flow to a chemical reaction which exhibits nonlinear front selection (for example the one of Hanna et al. [25]). Plane Poiseuille flow, Couette flow between rotating cylinders, or swirling jet experiments are systems where these experimental validation could also be achieved. In an experimental setup, a comparison of the growth size of the NG modes with the two generic scalings ($\ln(1/\epsilon)$ and $\epsilon^{-1/2}$) should allow a determination of whether the NG instability occurs while the system is C unstable or stable, or whether it occurs simultaneously at the C/A transition.

The very remarkable feature given by the proof of existence of an NG mode by matched asymptotic expansions is that the scaling laws as functions of the departure from the NG instability threshold are radically different when the NG threshold is linearly or nonlinearly determined. When the NG threshold coincides with the A threshold, the growth size Δx (a kind of downstream correlation scale) has been shown to vary as $\epsilon^{-1/2}$, ϵ being the departure from criticality. This power law contrasts sharply with the much stronger $\ln(1/\epsilon)$ variation of Δx obtained when the NG mode is nonlinearly determined and thus arises while the system is C unstable or S. Extension of the present study to the complex Ginzburg–Landau equation [34] shows that the same scaling holds and the theoretically derived law (with no free parameter) is shown to coincide exactly with the law observed by Büchel et al. [35] for the Taylor–Couette problem with throughflow and by Müller et al. [36] for the Rayleigh–Bénard problem with an added Poiseuille flow.

Acknowledgements

The authors are grateful to P. Manneville, P. Huerre and P. Weidman for their helpful comments on the manuscript.

Appendix A. Local behavior of solutions of Eq. (21) near the fixed points A_0, A_1, A_2

The study is restricted to the case $\mu > -1/4$.

At $A = A_0$, the linearized equation (21) gives

$$\frac{d^2 A}{dx^2} - U_0 \frac{dA}{dx} + \mu A = 0. \quad (\text{A.1})$$

The eigenvalues k^\pm are thus given by the expression

$$k^\pm = \frac{U_0}{2} \pm \frac{1}{2}(U_0^2 - 4\mu)^{1/2}. \quad (\text{A.2})$$

They are:

- complex conjugate with positive real part for $\mu > \mu^1 = U_0^2/4$ (A_0 is an unstable focus),
- real positive for $0 < \mu < \mu^1$ (A_0 is an unstable node),
- real and of opposite signs for $-1/4 < \mu < 0$ (A_0 is a saddle).

For $\mu = \mu^1$, A_0 is an improper node.

At $A = A_1$, we find the two eigenvalues k_1^\pm in the same way

$$k_1^\pm = \frac{U_0}{2} \pm \frac{1}{2} \left(U_0^2 - 8\sqrt{\mu + \frac{1}{4}} + 16\mu + 4 \right)^{1/2} \quad (\text{A.3})$$

They take the same value for $\mu = \mu_M(1 \pm \frac{2}{3}(1 - U_0^2)^{1/2} - \frac{1}{3}(1 - U_0^2))$. This equation bounds a domain of the parameter space (μ, U_0) in which A_1 is an unstable spiral point, whereas it is an unstable node out of this domain. On the boundary of this domain, A_1 is an improper node.

At $A = A_2$, The two eigenvalues k_2^\pm are given by the expression

$$k_2^\pm = \frac{U_0}{2} \pm \frac{1}{2} \left(U_0^2 + 8\sqrt{\mu + \frac{1}{4}} + 16\mu + 4 \right)^{1/2}. \quad (\text{A.4})$$

They are always real and of opposite signs (A_2 is always a saddle).

These results are reported on the Fig. 23.

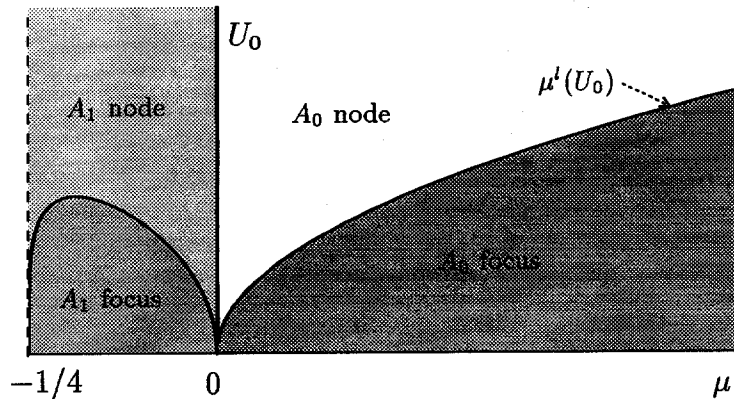


Fig. 23. Nature of the fixed points A_0, A_1, A_2 versus the parameters μ and U_0 . A_0 is an unstable focus in the dark gray domain, an unstable node in the white domain and a saddle for $\mu < 0$ (light and medium gray domain). A_1 is an unstable focus in the medium gray domain and an unstable node in the light gray domain. A_2 is a saddle everywhere.

Appendix B. Singular perturbation analysis of the subcritical Ginzburg–Landau equation in the vicinity of the curve $\mu = \mu^{\text{nl}}(U_0)$ for $U_0 < \sqrt{3}$

B.1. Scaling law $dA/dx(x = 0) = f(\epsilon)$ with $\epsilon = \mu - \mu^{\text{nl}}$

The absolute instability threshold is given by

$$\mu_A = \mu^{\text{nl}} = \mu_M \left(1 - \frac{2}{\sqrt{3}} U_0 - U_0^2 \right). \tag{B.1}$$

Throughout Appendix B we precise the dependence $A_2(\mu)$ only if necessary. Otherwise we use the notations $A_2 \equiv A_2(\mu^{\text{nl}})$ and $A_{2,\mu} \equiv dA_2/d\mu(\mu^{\text{nl}})$.

We seek a solution $u(A)$ of the Eq. (23) verifying boundary conditions (24). This function $u(A)$ is known for the value $\mu = \mu^{\text{nl}}$ (see Eq. (18)).

The order-1 equation (23) is compatible with a single boundary condition. We also assume the existence of an ϵ^β sized boundary layer in the neighborhood of A_0 in which an inner solution of the linearized equation (23) at $A = 0$ satisfies the boundary condition $u'(A_0) = U_0$ and out of which an outer solution of Eq. (23) satisfies the boundary condition $u(A_2(\mu)) = 0$.

Outer solution: Assuming that the solution $u(A)$ takes the following form:

$$u(A) \simeq u_0(A) + \epsilon u_1(A), \tag{B.2}$$

and expanding the second boundary condition $u(A_2(\mu^{\text{nl}} + \epsilon)) = 0$ and Eq. (23) in powers of ϵ , by comparison at each order we obtain:

– order 0

$$u_0 u_0' - U_0 u_0 + \mu^{\text{nl}} A + A^3 - A^5 = 0, \tag{B.3a}$$

$$u_0(A_2) = 0, \tag{B.3b}$$

– order 1

$$u_0 u_1' + u_0' u_1 - U_0 u_1 + A = 0, \tag{B.4a}$$

$$A_{2,\mu} u_0'(A_2) + u_1(A_2) = 0. \tag{B.4b}$$

The solution $u_0(A)$ is given by (see Eq. (18)):

$$u_0(A) = \frac{1}{\sqrt{3}} A (A_2^2 - A^2) \tag{B.5}$$

Upon substituting this solution in the system (B.4a) and (B.4b), and solving a first-order differential equation, we find

$$u_1(A) = A^{\lambda_1} (A_2^2 - A^2)^{\lambda_2} \sqrt{3} \int_{A_2}^A a^{-\lambda_1} (A_2^2 - a^2)^{-\lambda_2 - 1} da, \tag{B.6}$$

where

$$\lambda_1 = \frac{-1 + \sqrt{3}U_0}{1 + U_0/\sqrt{3}} \quad \text{and} \quad \lambda_2 = \frac{-1 - \sqrt{3}U_0}{1 + U_0/\sqrt{3}}. \tag{B.7}$$

Inner solution: The inner variable ξ is connected to the outer variable A through the relation

$$\xi = \frac{A}{\epsilon^\beta} \quad (\text{B.8})$$

with β as yet unknown. At the first order ϵ^β , the linearized Ginzburg–Landau equation at $A = A_0$ yields the equation for the inner solution $\xi(x)$.

$$\frac{d^2\xi}{dx^2} - U_0 \frac{d\xi}{dx} + \mu^{nl}\xi = 0. \quad (\text{B.9})$$

Using the notation $v(\xi) = d\xi/dx$, the condition $u'(A_0) = U_0$ yields

$$v'(0) = U_0 \quad (\text{B.10})$$

and the solution of Eq. (B.9) takes the form

$$\xi(x) = \frac{2v_0}{\sqrt{3} - U_0} (e^{r^+x} - e^{r^-x}), \quad (\text{B.11})$$

where $r^+ = (U_0 + \sqrt{3})/4$, $r^- = (3U_0 - \sqrt{3})/4$ and v_0 remains unknown since the second-order equation (B.9) is to be solved with only one boundary condition.

The next step is the matching of the outer and inner solutions. Let us introduce

$$\eta = \frac{A}{\epsilon^\alpha} = \xi \epsilon^{\beta-\alpha} \quad (\text{B.12})$$

into both solutions and expand the solutions in powers of ϵ in order to make the identification

$$u(A) \equiv \epsilon^\beta v(\xi). \quad (\text{B.13})$$

The expansion of the inner solution reads

$$v(\xi) = \frac{U_0 + \sqrt{3}}{4} \eta \epsilon^{\alpha-\beta} + v_0^{1-\lambda_1} \left(\frac{\sqrt{3} - U_0}{2} \right)^{\lambda_1} \eta^{\lambda_1} \epsilon^{(\alpha-\beta)\lambda_1}. \quad (\text{B.14})$$

The expansion of the outer solution yields

$$u(A) = \frac{A_2^2}{\sqrt{3}} \eta \epsilon^\alpha + \sqrt{3} A_2^{2\lambda_2} \eta^{\lambda_1} \epsilon^{\alpha\lambda_1+1} \int_0^{A_2} a^{-\lambda_1} (A_2^2 - a^2)^{-\lambda_2-1} da. \quad (\text{B.15})$$

Since $A_2^2/\sqrt{3} = (U_0 + \sqrt{3})/4$, the comparison at the order ϵ^α gives no information. The comparison at the following order yields the size of the boundary layer

$$\beta = \frac{1}{1 - \lambda_1} = \frac{\sqrt{3} + U_0}{2(\sqrt{3} - U_0)} \quad (\text{B.16})$$

and by insertion of the value v_0 , the sought scaling law reads

$$u(A_0) = v_0 \epsilon^\beta, \quad (\text{B.17})$$

where

$$v_0 = \left(A_2^{-1-\lambda_1} \sqrt{3} \left(\frac{\sqrt{3} - U_0}{2} \right)^{-\lambda_1} \int_0^1 a^{-\lambda_1} (1 - a^2)^{-\lambda_2-1} da \right)^\beta. \quad (\text{B.18})$$

Using the beta function [32], this expression may be succinctly written

$$v_0 = \frac{3^{\beta-1/2}}{2^\beta} A_2^{3-4\beta} \mathcal{B}^\beta \left(2 - \frac{1}{2\beta}; \frac{1}{2\beta} \right). \tag{B.19}$$

B.2. Scaling law $\Delta x = f(\epsilon)$ with $\epsilon = \mu - \mu^{nl}$

The characteristic size of the front linking A_0 to A_2 for $\mu = \mu^{nl} + \epsilon$ is calculated in two parts: in the first part Δx_i is related to the inner solution; one has to calculate x_i such as $\xi(x_i) = 1$; in the second part Δx_o is related to the outer solution and verifies $\Delta x_o = x_o - x_i$ where

$$A(x_i) = \epsilon^\beta \quad \text{and} \quad A(x_o) = 0.99 A_2(\mu). \tag{B.20}$$

The inner solution is given by expression (B.11). Thus, the first approximation of the inner characteristic size is given by the equation

$$\Delta x_i = x_i = \frac{4}{\sqrt{3} + U_0} \ln \left(\frac{\sqrt{3} - U_0}{2v_0} \right). \tag{B.21}$$

The value v_0 is given by solution of Eqs. (B.19) and (B.16).

The outer solution is given by the expression

$$\frac{dA}{dx} = u(A) = u_0(A) + \epsilon u_1(A). \tag{B.22}$$

Integrating the equation

$$\frac{dA}{u_0(A) + \epsilon u_1(A)} \simeq \frac{dA}{u_0(A)} - \epsilon \frac{u_1(A) dA}{u_0^2(A)} = dx \tag{B.23}$$

and neglecting terms of order ϵ , we obtain

$$\begin{aligned} \Delta x_o &= \int_{\epsilon^\beta}^{0.99 A_2(\mu)} \frac{\sqrt{3}}{A_2^2} \left(\frac{1}{A} + \frac{1}{2(A_2 - A)} - \frac{1}{2(A_2 + A)} \right) dA \\ &= \frac{\sqrt{3}}{A_2^2} \log \left(\frac{0.99 A_2}{\epsilon^\beta |1 - (0.99)^2 - 2\epsilon(0.99)^2 A_{2,\mu}/A_2|^{1/2}} \right), \end{aligned} \tag{B.24}$$

which yields the scaling law for the characteristic size by adding expressions (B.21) and (B.24), viz.,

$$\Delta x = \Delta x_i + \Delta x_o = \frac{\sqrt{3}}{A_2^2} (-\beta \log \epsilon + \log K), \tag{B.25}$$

where

$$K = \frac{0.992^\beta A_2^{4\beta} \mathcal{B}^{-\beta} (2 - 1/2\beta; 1/2\beta)}{\beta 3^\beta |1 - (0.99)^2 - 2\epsilon(0.99)^2 A_{2,\mu}/A_2|^{1/2}}. \tag{B.26}$$

\mathcal{B} is again the beta function.

Appendix C. Singular perturbation analysis of the *subcritical* Ginzburg–Landau equation in the vicinity of $\mu = \mu^1(U_0)$ for $U_0 > \sqrt{3}$

C.1. *Scaling laws* $dA/dx(0) = f(\epsilon)$ and $\Delta x = f(\epsilon)$ with $\epsilon = \mu - \mu^1$ and $U_0 > \sqrt{3}$

The absolute instability threshold is given by

$$\mu_A = \mu^1 = U_0^2/4. \quad (\text{C.1})$$

Throughout Appendix C we precise the dependence $A_2(\mu)$ only if necessary. Otherwise we use the notations $A_2 \equiv A_2(\mu^1)$ and $A_{2,\mu} \equiv dA_2/d\mu(\mu^1)$.

We seek a solution of Eq. (23) representing the stable manifold of A_2 as a series in the form

$$u(A) = - \sum_{k=1}^{+\infty} v_k(\mu) (A_2(\mu) - A)^k. \quad (\text{C.2})$$

The boundary condition $u(A_2(\mu)) = 0$ is automatically verified since there is no zero-order term in the series. In order to calculate the coefficients v_k , one has to satisfy Eq. (23) at each order. The coefficients v_k are thus calculated from v_1 by the following recurrence formulas:

$$v_1 = \frac{U_0}{2} - \frac{1}{2}(U_0^2 - 4\Gamma_1)^{1/2}, \quad (\text{C.3a})$$

$$v_{2k} = \frac{(2k+1) \left(\sum_{n=2}^k v_n v_{2k+1-n} \right) + \Gamma_{2k}}{U_0 - (2k+1)v_1}, \quad (\text{C.3b})$$

$$v_{2k-1} = \frac{2k \left(\sum_{n=2}^{k-1} v_n v_{2k-n} + v_k^2/2 \right) + \Gamma_{2k-1}}{U_0 - 2kv_1}. \quad (\text{C.3c})$$

The coefficients Γ_k depend on the shape of the potential and are given by

$$\Gamma_k = \frac{(-1)^k}{k!} \frac{d^{k+1} \mathcal{V}}{dA^{k+1}}(A_2(\mu)). \quad (\text{C.4})$$

For the particular value $\mu^1 = U_0^2/4$, Eq. (C.2) represents the outer solution displayed by the continuous line in Figs. 4(a) and (d) at the absolute instability threshold. Therefore, we do not apply the boundary condition at $A = A_0$. In the inner layer, the inner variable is ξ and the inner solution is calculated as a function of the departure from the criticality $\epsilon = \mu - \mu^1$, as a solution of Eq. (23) linearized about $A = A_0$ with the boundary condition $\xi(0) = 0$:

$$\xi(x) = \frac{v_0}{\sqrt{\epsilon}} \exp\left(\frac{U_0}{2}x\right) \sin(\sqrt{\epsilon}x). \quad (\text{C.5})$$

v_0 is the slope at the origin of this solution $v(\xi) = d\xi/dx$ and is not yet determined since only one boundary condition has been applied to a second-order equation. The matching between the inner solution $v(\xi) = d\xi/dx$ and the outer solution $u(A) = dA/dx$ allows a determination of v_0 . One has to choose the following scaling between the inner variable and the outer variable in order to make the matching tractable

$$\xi = \epsilon^{-1} \exp\left(\frac{U_0\pi}{2\sqrt{\epsilon}} - \frac{U_0A}{2v_0\epsilon}\right) A. \quad (\text{C.6})$$

In other words, the inner solution (C.5) reaches its maximum at a value x_i close to $\pi/\sqrt{\epsilon}$ and both inner and outer solutions overlap for $x \simeq x_i$. Since the contribution of the outer solution (C.2) to the growth size scales like $\log \epsilon$, the dominant term for the characteristic size is given by

$$\Delta x \simeq \frac{\pi}{\sqrt{\epsilon}}. \tag{C.7}$$

We also choose an intermediate variable η such that

$$A = \eta \epsilon^\alpha \quad \text{with } \frac{1}{2} < \alpha \leq 1. \tag{C.8}$$

Expanding the inner and outer solutions in increasing powers of ϵ , we obtain the inner solution as

$$v(\xi) = \left(\frac{U_0}{2} \eta \epsilon^\alpha - v_0 \epsilon \right) \epsilon^{-1} \exp\left(\frac{U_0 \pi}{2\sqrt{\epsilon}} - \frac{U_0 \eta \epsilon^{\alpha-1}}{2v_0} \right), \tag{C.9}$$

and for the outer solution one finds

$$u(A) = - \sum_{k=1}^{+\infty} v_k(\mu^1) A_2^k + \left(\sum_{k=1}^{+\infty} v_k(\mu^1) k A_2^{k-1} \right) \eta \epsilon^\alpha - \sum_{k=1}^{+\infty} \left(\frac{dv_k}{d\mu}(\mu^1) A_2^k + k v_k(\mu^1) A_{2,\mu} A_2^{k-1} \right) \epsilon. \tag{C.10}$$

We use the following notations:

$$w_k = v_k(\mu^1) A_2^{k-3} \quad \text{and} \quad z_k = \frac{dv_k}{d\mu}(\mu^1) A_2^k. \tag{C.11}$$

The term-by-term identification of the coefficients of the expansion in ϵ gives:

– first solvability condition (order 0):

$$\sum_{k=1}^{+\infty} w_k = 0 \quad \text{if } U_0 > \sqrt{3}, \quad \sum_{k=1}^{+\infty} w_k \neq 0 \quad \text{otherwise,} \tag{C.12}$$

– second solvability condition (order ϵ^α):

$$\sum_{k=1}^{+\infty} k w_k = \frac{U_0}{2A_2^2} \tag{C.13}$$

– sought after value of v_0 (order ϵ):

$$v_0 = \sum_{k=1}^{+\infty} (z_k + k w_k A_2^2 A_{2,\mu}). \tag{C.14}$$

The scaling law for $u(0) = dA/dx(x=0)$ then reads

$$u(0) = v_0 \epsilon \exp\left(-\frac{U_0 \pi}{2\sqrt{\epsilon}} \right). \tag{C.15}$$

The numerical values obtained for Eqs. (C.12)–(C.14) are shown in Table 1 as functions of the number of terms in the series for $U_0 = 2$. The convergence of the series is relatively slow. We find $\sum_1^N w_k \simeq 10^{-8}$ and $(2A_2^2/U_0) \sum_1^N k w_k \simeq 0.96$ for $N = 40\,000$ terms. The solvability conditions seem, however, to be verified.

Table 1

N	$-\sum_{k=1}^N w_k$	$(2A_2^2/U_0) \sum_{k=1}^N kw_k$	$\sum_{k=1}^N (z_k + kw_k A_2^2 A_{2,\mu})$
200	7.551×10^{-6}	0.9492	3.828×10^{-3}
400	3.519×10^{-6}	0.9510	1.831×10^{-3}
600	2.254×10^{-6}	0.9520	1.192×10^{-3}
800	1.644×10^{-6}	0.9526	8.798×10^{-4}
1000	1.287×10^{-6}	0.9531	6.953×10^{-4}
2000	6.035×10^{-7}	0.9547	3.356×10^{-4}
4000	2.834×10^{-7}	0.9561	1.625×10^{-4}
6000	1.823×10^{-7}	0.9569	1.064×10^{-4}
8000	1.333×10^{-7}	0.9575	7.891×10^{-5}
10 000	1.046×10^{-7}	0.9579	6.257×10^{-5}
20 000	4.938×10^{-8}	0.9591	3.048×10^{-5}
40 000	2.333×10^{-8}	0.9603	1.488×10^{-5}

Appendix D. Singular perturbation analysis of the supercritical Ginzburg–Landau equation in the vicinity of $\mu = \mu^1(U_0)$

D.1. Scaling law $dA/dx(0) = f(\epsilon)$ with $\epsilon = \mu - \mu^1$

The absolute instability threshold is given by $\mu_A = \mu^1 = U_0^2/4$. The calculation of the scaling law is the same as in the subcritical case with $U_0 > \sqrt{3}$. We follow the same approach. We seek a solution of the equation

$$uu' - U_0u + \mu A - A^3 = 0 \quad (\text{D.1})$$

as a series similar to (C.2). The coefficients v_k are calculated using formulas (C.3a)–(C.3c). The inner solution takes the same form as in Eq. (C.5). In order to do the matching, the scaling law between the inner and outer variable has to be chosen in the form (C.6). The matching between the solutions is done by expanding the inner and outer solutions at orders 0, ϵ^α , and ϵ (with $A = \eta\epsilon^\alpha$). Here we use the notations

$$w_k = v_k(\mu^1) A_2^{k-2}(\mu^1) \quad \text{and} \quad z_k = \frac{dv_k}{d\mu}(\mu^1) A_2^k(\mu^1), \quad (\text{D.2})$$

and by identifying the expansions of inner and outer solutions at each order, we obtain:

– at the order zero

$$\sum_{k=1}^{+\infty} w_k = 0, \quad (\text{D.3})$$

– at the order ϵ^α

$$\sum_{k=1}^{+\infty} kw_k = 1, \quad (\text{D.4})$$

– at the order ϵ

$$v_0 = \sum_{k=1}^{+\infty} \left(z_k + \frac{kw_k}{2} \right). \quad (\text{D.5})$$

Table 2

N	$-\sum_{k=1}^N w_k$	$\sum_{k=1}^N kw_k$	$\sum_{k=1}^N (z_k + kw_k/2)$
200	8.117×10^{-5}	0.860	2.895
400	3.419×10^{-5}	0.873	2.946
600	2.072×10^{-5}	0.879	2.971
800	1.456×10^{-5}	0.884	2.987
1000	1.109×10^{-5}	0.887	2.998
2000	4.789×10^{-6}	0.895	3.029
4000	2.087×10^{-6}	0.903	3.055
6000	1.289×10^{-6}	0.907	3.068
8000	9.178×10^{-7}	0.909	3.077
10 000	7.056×10^{-7}	0.911	3.083
20 000	3.133×10^{-7}	0.917	3.102
40 000	1.400×10^{-7}	0.921	3.118

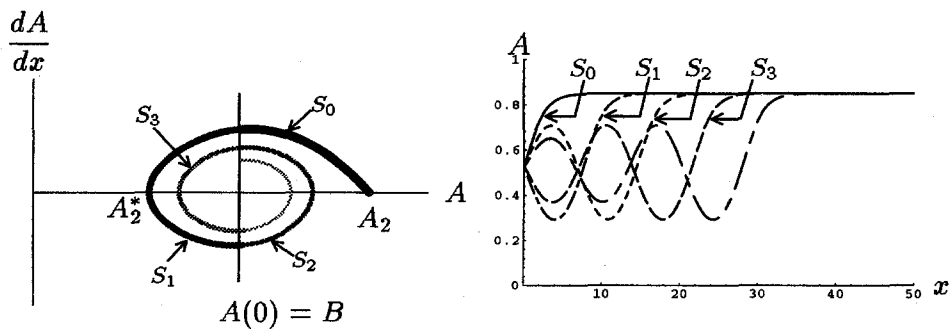
Eqs. (D.3) and (D.4) are solvability conditions and Eq. (D.5) then yields v_0 . The sought scaling law takes exactly the same form as in the subcritical case, viz.

$$u(0) = v_0 \epsilon \exp\left(-\frac{U_0 \pi}{2\sqrt{\epsilon}}\right). \tag{D.6}$$

Table 2 shows the numerical values obtained for the solvability conditions and the calculation of v_0 as functions of the number of terms in the series for the advection velocity $U_0 = 1$. The convergence of the series is relatively slow. For $N = 40\,000$ terms, we find $\sum_1^N w_k \simeq 10^{-7}$ and $\sum_1^N kw_k \simeq 0.92$. The solvability conditions seem, however, to be verified.

Appendix E. Multiplicity of solutions

Note that in the NC region and in the NS region, there may exist several steady solutions of Eq. (1) with potential density (2) satisfying the required boundary conditions $A(0) = B$ with either $A(+\infty) = A_2$ or $A(+\infty) = A_0$,



(a) Phase portrait.

(b) Forced solutions S_0, S_1, S_2 versus x .

Fig. 24. Multiplicity of forced solutions in the NC region for $\mu < 0$. Only S_0 verifies steady Ginzburg–Landau equation with boundary conditions $A(0) = B$ and $A(+\infty) = A_2$ without oscillating around A_1 .

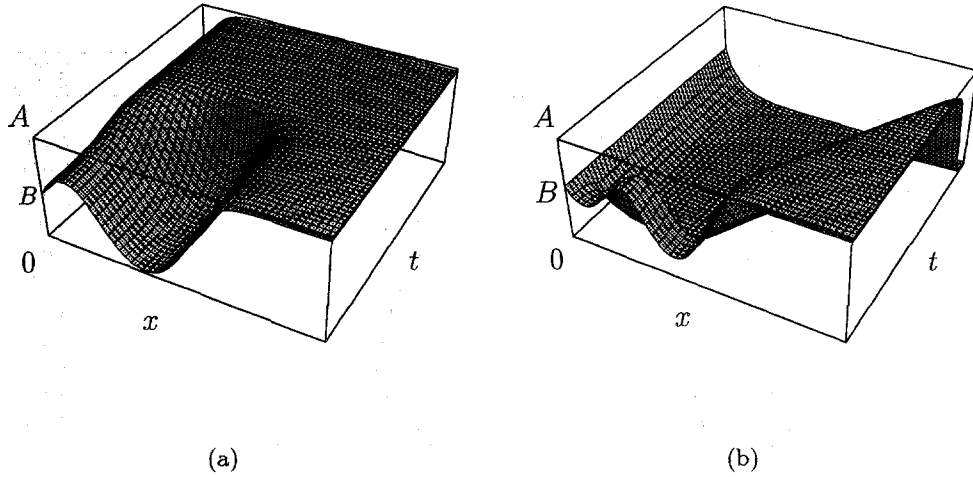


Fig. 25. Simulation in the NC region. (a) The starting solution crosses twice zero. $B = A_1$; $U_0 = 0.1$; $\mu = \mu_A - 0.01 = -0.164$. The system relaxes to the solution S_0 of Fig. 24 asymptotic to A_2 . (b) The starting solution crosses three times zero. $B = A_1$; $U_0 = 0.1$; $\mu = -0.164$. The system relaxes to the solution asymptotic to A_0 which does not oscillate around A_1 .

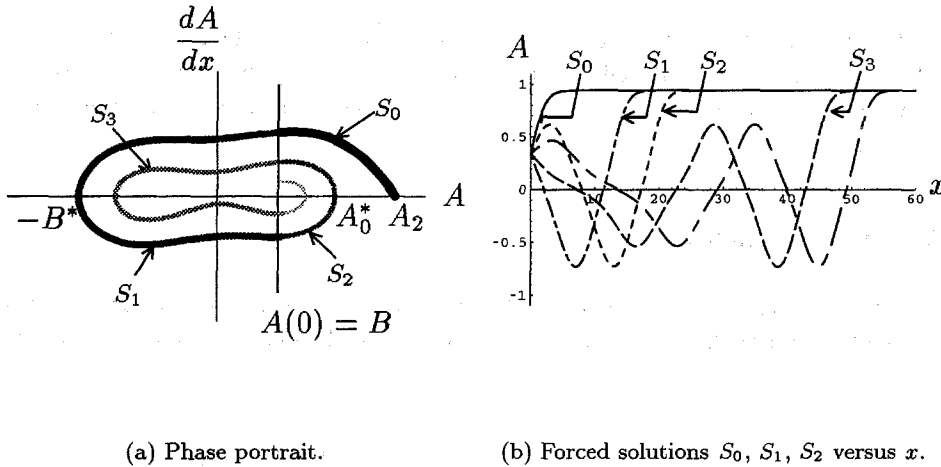


Fig. 26. Multiplicity of forced solutions in the NG region for $\mu < 0$. Only S_0 verifies steady Ginzburg–Landau equation with boundary conditions $A(0) = B$ and $A(+\infty) = A_2$ without oscillating around B .

and oscillating around $A = A_1$. An example of multiplicity of solutions is shown in Fig. 24. A necessary condition for multiple solutions is that the stable manifold of A_2 (or A_0) oscillates around the amplitude A_1 . For example, if $\mu < 0$, in the region of parameter space where A_1 is an unstable focus (see Appendix A) multiple solutions asymptotic to A_2 (or A_0) exist if $B > A_2^*$ (or $B < A_0^*$); when A_1 is an unstable node or when $\mu > 0$, there exists only one solution asymptotic to A_2 (or A_0) at $+\infty$.

In the simulation displayed in Fig. 25, an oscillating solution of Eq. (21) such that $A(0) = B$ and $A(+\infty) = A_2$ becomes unstable and evolves to the steady solution without oscillation, that verifies the same boundary conditions. All numerical simulations we have undertaken indicate that oscillating forced solutions are unstable. Depending on the initial solution, they evolve either to the steady solution satisfying $A(+\infty) = A_2$ with no oscillations (Fig. 25(a)), or to the steady solution satisfying $A(+\infty) = A_0$ but still without oscillation (Fig. 25(b)).

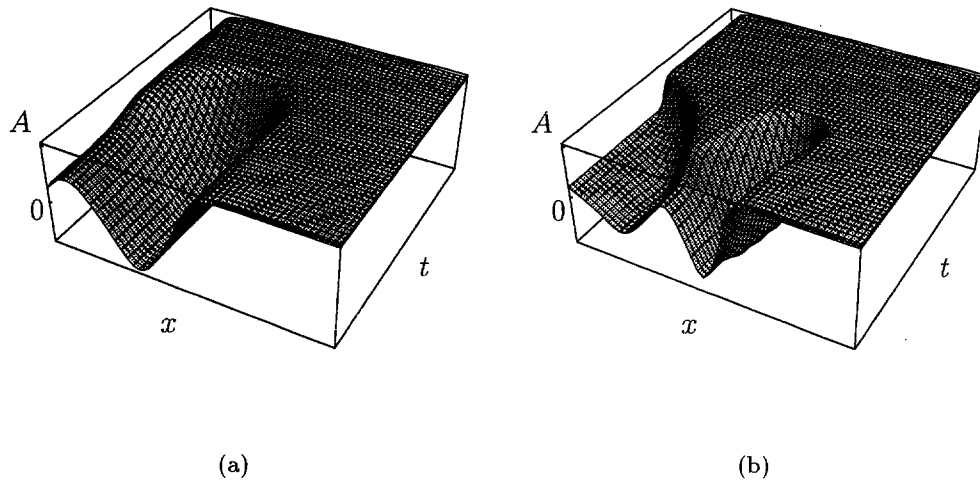


Fig. 27. Simulation in the NG region. (a) The starting solution crosses twice zero. $B = 0.25$; $U_0 = 0.1$; $\mu = 0.001$. (b) The starting solution crosses three times zero. $B = 0.2$; $U_0 = 0.1$; $\mu = -0.05$. In (a) and (b), the system relaxes to the solution S_0 of Fig. 26(b) asymptotic to A_2 .

In the NG region, there may also exist several steady solutions of Eq. (1) with potential density (2) such that $A(0) = B$ and $A(+\infty) = A_2$ as sketched in Fig. 26.

All temporal simulations indicate that only the non-oscillating solutions are stable (Fig. 27): For the parameter setting $U_0 = 0.1$ and $\mu = 0.001$ ($\mu = -0.05$), the solution S_2 (S_3) oscillating twice in Fig. 26(a) (three times in Fig. 26(b)) evolves to the solution S_0 with no oscillation.

References

- [1] P. Huerre and P.A. Monkewitz, Local and global instabilities in spatially developing flows, *Ann. Rev. Fluid Mech.* 22 (1990) 473.
- [2] A. Bers, in: *Physique des Plasmas*, eds. C. DeWitt and J. Peyraud (Gordon and Breach, New York, 1975).
- [3] M.C. Cross and P.C. Hohenberg, Pattern formation outside of equilibrium, *Rev. Mod. Phys.* 65 (1993) 851.
- [4] J.M. Chomaz, P. Huerre and L.G. Redekopp, Bifurcations to local and global modes in spatially developing flows, *Phys. Rev. Lett.* 60 (1988) 25.
- [5] J.M. Chomaz, P. Huerre and L.G. Redekopp, The effect of nonlinearity and forcing on global modes, in: *New Trends in Nonlinear Dynamics and Pattern-Forming Phenomena*, eds. P. Coulet and P. Huerre (Plenum Press, New York, 1990).
- [6] J.M. Chomaz, P. Huerre and L.G. Redekopp, A frequency selection criterion in spatially developing flows, *Stud. Appl. Math.* 84 (1991) 119.
- [7] P.A. Monkewitz, P. Huerre and J.M. Chomaz, Global linear stability analysis of weakly non parallel shear flows, *J. Fluid Mech.* 251 (1993) 1.
- [8] S. Le Dizès, P. Huerre, J.M. Chomaz and P.A. Monkewitz, Linear global modes in spatially developing media, *Phil. Trans. R. Soc. Lond. A* 354 (1996) 169.
- [9] R.E. Hunt, Spatially varying flows with localized forcing, Ph.D. Thesis.
- [10] R.E. Hunt and D.G. Crighton, Instability of flows in spatially developing media, *R. Soc. Lond. A* 435, 109.
- [11] K.R. Sreenivasan, S. Raghun and D. Kyle, Absolute instability in variable density round jets, *Exp. Fluids* 7 (1989) 309.
- [12] P.J. Strykowski and D.L. Niccum, The influence of velocity and density ratio on the dynamics of spatially developing mixing layers, *Phys. Fluids A* 4 (1992) 770.
- [13] S. Le Dizès, P. Huerre, J.M. Chomaz and P.A. Monkewitz, Nonlinear stability analysis of slowly diverging flows: Limitations of the weakly nonlinear approach, in: *Proc. IUTAM Symp. on bluff-body wakes, dynamics and instabilities*, eds. H. Eckelmann, J.M.R. Graham, P. Huerre and P.A. Monkewitz (Springer, Berlin, 1997).
- [14] J.M. Chomaz, Absolute and convective instabilities in nonlinear systems, *Phys. Rev. Lett.* 69 (1992) 1931.
- [15] G. Dec, Dynamical properties of propagating front solutions of the amplitude equations, *Physica D* 15 (1985) 295.

- [16] G. Dee, Propagation into an unstable state, *J. Statist. Phys.* 39 (1985) 705.
- [17] E. Ben-Jacob, H. Brand, G. Dee, L. Kramer and J.S. Langer, Pattern propagation in nonlinear dissipative systems, *Physica D* 14 (1985) 348.
- [18] W. van Saarloos and P.C. Hohenberg, Fronts, pulses, sources and sinks in generalized complex Ginzburg-Landau equations, *Physica D* 56 (1992) 303.
- [19] W. van Saarloos, Front propagation into unstable states: Marginal stability as a dynamical mechanism for velocity selection, *Phys. Rev. A* 37 (1988) 211.
- [20] W. van Saarloos, Front propagation into unstable states. II. Linear versus nonlinear marginal stability and rate of convergence, *Phys. Rev. A* 39 (1989) 6367.
- [21] A. Couairon and J.M. Chomaz, Global Instability in fully nonlinear systems, *Phys. Rev. Lett.* 77 (1996) 4015.
- [22] J. Fineberg and V. Steinberg, Vortex-front propagation in Rayleigh-Bénard convection, *Phys. Rev. Lett.* 58 (1987) 1332.
- [23] G. Ahlers and D.S. Cannel, Vortex-front propagation in rotating Couette-Taylor flow, *Phys. Rev. Lett.* 50 (1983) 1583.
- [24] M. Lücke, M. Mihelcic and K. Wingerath, Front propagation and pattern formation of Taylor vortices growing into unstable circular Couette flow, *Phys. Rev. A* 31 (1985) 396.
- [25] A. Hanna, A. Saul and K. Showalter, Detailed studies of propagating fronts in the iodate oxydation of arsenous acid, *J. Am. Chem. Soc.* 104 (1982) 3838.
- [26] D.G. Aronson and H.F. Weinberger, Multidimensional nonlinear diffusion arising in population genetics, *Adv. Math.* 30 (1978) 33.
- [27] P. Palfy-Muhoray, H.J. Yuan, B.J. Frisken and W. van Saarloos, in: *Nonlinear Evolution of Spatio-temporal Structures in Dissipative Continuous Systems*, eds. F.H. Busse and L. Kramer (Plenum Press, New York, 1990).
- [28] J.D. Gunton, M. San Miguel and P.S. Sahni, The dynamics of first-order phase transitions, in: *Phase Transitions and Critical Phenomena*, eds. C. Domb and J.L. Lebowitz, Vol. 8 (Academic Press, New York, 1983).
- [29] J.A. Powell, A.C. Newell and C.K.R.T. Jones, Competition between generic and nongeneric fronts in envelope equations, *Phys. Rev. A* 44 (1991) 3636.
- [30] C.M. Bender and S.A. Orszag, *Advanced Mathematical Methods for Scientists and Engineers* (McGraw-Hill, New York, 1978).
- [31] P. Coullet, L. Gil and D. Repaux, Defects and subcritical bifurcations, *Phys. Rev. Lett.* 62 (1989) 2957.
- [32] M. Abramowitz and I.A. Stegun, *Handbook of Mathematical Functions* (Dover, New York).
- [33] V. Hakim, in: *Hydrodynamics and nonlinear instabilities*, Cambridge University Press, to be published.
- [34] A. Couairon and J.M. Chomaz, Pattern selection in the presence of a cross flow, *Phys. Rev. Lett.*, submitted.
- [35] P. Büchel, M. Lücke, D. Roth and R. Schmitz, Pattern selection in the absolutely unstable regime as a nonlinear eigenvalue problem: Taylor vortices in axial flow, *Phys. Rev. E* 53 (1996) 4764.
- [36] H.W. Müller, M. Lücke and M. Kamps, Convective Patterns in Horizontal flow, *Europhys. Lett.* 10 (1989) 451; Transversal convection patterns in horizontal shear flow, *Phys. Rev. A* 45 (1992) 3714.
- [37] J. Guckenheimer and P. Holmes, *Nonlinear Oscillations, Dynamical Systems, and Bifurcations of Vector Fields* (Springer, Berlin, 1983).
- [38] D.G. Aronson and H.F. Weinberger, Nonlinear diffusion in population genetics, combustion, and nerve propagation, in: *Partial Differential Equations and Related Topics, Lecture Notes in Mathematics*, Vol. 446 (Springer, New York, 1975) pp. 5–49.